2-3-2016

Evaluation of Near-Infrared Contrast Agents for Cancer Detection using Optical Imaging Techniques

Akram Abuteen
akram.abuteen@uconn.edu

Evaluation of Near-Infrared Contrast Agents for Cancer Detection using Optical Imaging Techniques

Akram Abuteen, PhD

University of Connecticut, 2016

Abstract

Breast cancer is the second most common type of cancer among women, with an estimated 2.8 million diagnosed in the United States. Many cancers cannot be detected by their intrinsic vascular contrast, especially in their early stages. This necessitates the use of an exogenous contrast agent. Photoacoustic Imaging (PAI) and Fluorescence imaging (FI) are promising non-invasive *in vivo* cancer diagnostic methods. To further improve the tumor to background contrast, researchers are investigating various exogenous contrast agents for PAI and fluorescence imaging that target tumor vasculature and hypoxia.

This dissertation is structured into two main sections. In the first part, the evaluation of several novel porphyrin dyes has been presented as PAI contrast agents in direct comparison to the commonly used indocyanine green (ICG). Imaging of a sub-mm target containing quinoline-annulated porphyrin up to 2 cm depth in a tissue-like matrix exceeds the performance of imaging the similar target containing ICG, which suggests the use of quinoline-annulated porphyrins as potential contrast agents for cancer detection using PAI. The second part of the dissertation reports an investigation of the unsubstituted imidazole derivative as well as the 4-nitroimidazole ICG-conjugate for targeting tumor hypoxia. The performance of 4-nitroimidazole dye by imaging tumor cells *in vitro* and animals *in vivo* were validated, and the results with the 2-nitroimidazole dye were compared, using the imidazole derivative as the reference. The results demonstrated the efficacy of 4-nitroimidazole-ICG as a hypoxia targeting fluorescence probe and

suggest the use of 4-nitroimidazole dye-conjugate as a hypoxia probe with a significant cost reduction in the synthesis.

Evaluation of Near-Infrared Contrast Agents for Cancer Detection using Optical Imaging Techniques

Akram Abuteen

B.S. in Electrical and Computer Engineering, Arab Academy for Science and Technology, Alexandria, Egypt, 1994

M.S. in Computer Engineering, University of Bridgeport, 1999

A Dissertation

Submitted in Partial Fulfillment of the

Requirements for the Degree of

Doctor of Philosophy

at the

University of Connecticut

2016

APPROVAL PAGE

Doctor of Philosophy Dissertation

Evaluation of Near-Infrared Contrast Agents for Cancer Detection using Optical Imaging Techniques

Presented by

Akram Abuteen, B.S., M.S.

Major Advisor _____
Prof. Quing Zhu

Associate Advisor _____
Prof. Rajeev Bansal

Associate Advisor _____
Prof. Christian Brueckner

Associate Advisor _____
Prof. Patrick Kumavor

Associate Advisor _____
Prof. Michael Smith

University of Connecticut
2016

To my parents

Issa Abuteen and Ruqayya Jaidi

Acknowledgements

I would like to thank my advisor Prof. Quing Zhu for her support through all these years I spent at UCONN. Her words “Your persistence will lead you to completion” are what kept me going. Pursuing a PHD degree on a part time basis was not an easy task. But without the help of so many people, this work would have not been possible. First I want to start with my parents whom no gratitude suffices to show how much I appreciate all the help and passion they showed at all my life stages. I would like to thank my co-advisors, Prof. Bansal, Prof. Brueckner, Prof. Smith and Prof. Patrick for all their support and advice. Thanks go also to my wonderful wife Noranita Mohd Yusof whom showed endless support and perseverance along this journey. Thanks to my beloved angel Amani Aouamria. Thanks to all my friends who have encouraged me every step of the way.

Table of Contents

List of Figures

List of Tables

Publications

Peer-Reviewed Journal Papers

1 **Akram Abuteen**, Saeid Zanganeh, Joshua Akhigbe, Lalith P. Samankumara, Andres Aguirre, Nrusingh Biswal, Marcel Braune, Anke Vollertsen, Beate Roeder, Christian Brueckner and Quing Zhu (2013). "The evaluation of NIR-absorbing porphyrin derivatives as contrast agents in photoacoustic imaging." Phys Chem Chem Phys 15(42): 18502-18509.

2 **Akram Abuteen**, Feifei Zhou, Christopher Dietz, Innus Mohammad, Michael B. Smith, Quing Zhu (2016). "Synthesis of a 4-nitroimidazole indocyanine dye-conjugate and imaging of tumor hypoxia in BALB/c tumor-bearing female mice." Dyes and Pigments 126: 251-260.

3 Zhou, Feifei, Zanganeh, Saeid, Mohammad, Innus, Dietz, Christopher, **Abuteen, Akram**, Smith, Michael B., Zhu, Quing (2015). "Targeting tumor hypoxia: a third generation 2-nitroimidazole-indocyanine dye-conjugate with improved fluorescent yield." Org Biomol Chem 13(46): 11220-11227.

Chapter 1

Breast Cancer and Optical Imaging

1-1 Introduction

1-1.1 Overview

Breast cancer is the second most common type of cancer, with an estimated 2.8 million diagnosed breast cancer patients in the United States. The mortality rate is estimated at 17% in the 232,340 patients diagnosed in 2013 [1]. This mortality rate can be drastically reduced by early detection, however many cancers cannot be detected by their intrinsic vascular contrast, especially in their early stages [2, 3]. This necessitates the use of an exogenous contrast agent. Different contrast agents such as nanoparticles, gold nanoparticles containing organic dyes such as ICG (indocyanine green) and porphysomes have been used [4-6]. Near-infrared (NIR) optical imaging distinguishes itself from other imaging modalities by its features such as non-ionizing radiation, noninvasive technology for imaging and quantifying vascularity, multimodal imaging, cost effectiveness and its ability for real time data acquisition. Near Infra-red imaging have better tissue penetration, less autofluorescence, and large Stokes shifts. Near-infrared fluorescence imaging and the use of nitroimidazoles as exogenous probes has received great attention because of their unique behavior in hypoxic environments owing to their high electron affinity [15-17]. Nonetheless, Photoacoustic Imaging (PAI) and Fluorescence imaging are promising non-invasive *in vivo* diagnostic methods. PAI provides optical contrast at ultrasonic imaging resolution. To further improve the optical contrast, researchers are investigating various exogenous contrast agents for PAI and fluorescence imaging that target tumor vascularity with

appropriate tumor-specific ligands and target tumor hypoxia [7-10]. PAI has an advantage over other imaging modalities such as MRI and CT by its non-ionizing effect, the absence of radioactivity, and its combined high ultrasonic resolution and high optical contrast.

This research focuses on the identification and evaluation of next generation novel contrast agents that may significantly enhance the effectiveness of PAI in early visualization of breast cancer. The overarching goal of this research is to increase the optical contrast in PAI and improve tumor hypoxia targeting using fluorescence imaging modality, to enable early detection of cancerous tumors resulting in decrease or morbidity and mortality in patients.

1-1.2 Photoacoustic principle

Photoacoustic phenomena was first described by Alexander Graham Bell in 1880 [12]. The lack of strong light sources caused further research on the application to cease soon after. With the development of lasers in the early 1970s, photoacoustic spectroscopy was revived. Lasers provided high intensity light at a tunable frequency, which allowed an increase in sound amplitude and sensitivity. The basic principle of the photoacoustic phenomena can be described as a chromophore or a particle absorbs a pulsed radiation energy, the absorbed energy is converted into heat and the temperature of the object increases. This rise in temperature causes a thermal expansion, generating an acoustic wave in the medium [11]. By detecting these acoustic waves using an ultrasound transducer and processing them using a beamforming algorithm, photoacoustic images are formed. PAI can reconstruct light absorption map inside the biological

tissue. The photoacoustic wave generation is described by the general photoacoustic equation [23]

$$\left(\nabla^2 - \frac{1}{v_s^2}\frac{\partial^2}{\partial t^2}\right) p\left(\mathbf{r}, t\right) = -\frac{\beta}{C_P}\frac{\partial H\left(\mathbf{r}, t\right)}{\partial t} \quad (1)$$

where p(r, t) denotes the acoustic pressure at location r and time t, v_s denotes the speed of sound (~1480 m/s in water), β denotes the thermal coefficient of volume expansion (~4×10^{-4} K^{-1} for muscle), H is the heating function defined as the thermal energy converted per unit volume and per unit time; it is related to the optical absorption coefficient μ_a and fluence rate Φ by $H = \mu_a\Phi$ and C_p [~4000 J/(kg·K) for muscle] denote the specific heat capacity at constant pressure. The left-hand side of equation (1) describes the wave propagation, whereas the right-hand side represents the source term. For a short laser pulse that satisfies the assumption that the laser pulse duration is less than the acoustic confinement time, which is less than the thermal confinement time, the following thermal equation holds:

$$\rho C_V \frac{\partial T(\mathbf{r}, t)}{\partial t} = H(\mathbf{r}, t), \quad (2)$$

where T denotes the temperature rise and Cv denote the specific heat capacity at constant volume.

Using the forward solution, the general photoacoustic equation can be solved by the Green's function approach which is defined as the response to a spatial and temporal impulse source term, assuming an infinite space, where no boundary exists

$$G(\mathbf{r},t;\mathbf{r}',t') = \frac{\delta(t-t'-|\mathbf{r}-\mathbf{r}'|/v_s)}{4\pi|\mathbf{r}-\mathbf{r}'|} \quad , (3)$$

which represents an impulse diverging spherical wave, where r' and t' denote the source location and time, respectively. Applying the Green's function approach, we get

$$p(\mathbf{r},t) = \int_{-\infty}^{t^+} dt' \int d\mathbf{r}' G(\mathbf{r},t;\mathbf{r}',t') \frac{\beta}{\kappa v_s^2} \frac{\partial^2 T(\mathbf{r}',t')}{\partial t'^2} \quad , (4)$$

which represents the pressure in response to an arbitrary source. Here, κ denotes the isothermal compressibility. By substituting, simplifying and approximating the heat function $H_t(t')=\delta(t')$ we get

$$p(\mathbf{r},t) = \frac{1}{4\pi v_s^2} \frac{\partial}{\partial t} \left[\frac{1}{v_s t} \int d\mathbf{r}' p_0(\mathbf{r}') \delta\left(t - \frac{|\mathbf{r}-\mathbf{r}'|}{v_s}\right) \right] . \quad , (5)$$

which can be used to compute photoacoustic pressure generated by an arbitrarily heterogeneous optically absorbing object.

1-1.3 Fluorescence Imaging

In fluorescence imaging, photons are absorbed by a fluorescent molecule, and emits light (fluoresces) at a longer wavelength in order to return from its excited state to its ground energy state in a certain period of time. This emitted light can be captured with CCD (charge-couple device) camera or detectors, and the quality of the detection will rely mainly on the capacity to filtrate the emitted photons from the illumination light. The absorption of light is connected with

an electronic transition from the ground state to an excited stated of the molecule. The light passing through a layer of thickness *d* is attenuated and described as

$$I(\lambda) = I_o \exp(-\mu_a d) = I_o \, 10^{-\varepsilon\lambda \, Cab \, d}, \quad (6)$$

where $I(\lambda)$ is the transmitted light intensity, I_o is the incident intensity, $\varepsilon\lambda$ is the molar extinction coefficient and C_{ab} is the concentration of the absorbing molecule [13]. In scattering samples, the absorbing coefficient μ_a and the scattering coefficient μ_s sums up. The molecule fluorescence intensity or quantum flux corresponds to the intensity equation

$$I_F(\lambda) = I_o \left[1 - 10^{-\varepsilon\lambda \, Cab \, d}\right] \Phi_F \frac{\Omega}{\pi}, \quad (7)$$

where Φ_F is the fluorescence quantum yield and Ω the angle of detection of the isotropic fluorescence radiation. In case of thin samples such as cells or biopsies with thickness in the micrometer range the fluorescence intensity equation can be approximated as

$$I_F(\lambda) = I_o \ln 10^{-\varepsilon\lambda \, Cab \, d} \, \Phi_F \frac{\Omega}{\pi}, \quad (8)$$

which implies that fluorescence intensity is proportional to the concentration and the fluorescence quantum yield of the absorbing molecule.

The fluorescence quantum yield (Φ_F) is the ratio of photons absorbed to photons emitted through fluorescence. In other words the quantum yield gives the probability of the excited state being deactivated by fluorescence rather than by another, non-radiative mechanism. The most reliable method for recording the quantum yield is the comparative method [14], which involves

the use of well characterized standard samples with known fluorescence quantum yield values. Essentially, solutions of the standard and test samples with identical absorbance at the same excitation wavelength can be assumed to be absorbing the same number of photons. Hence, a simple ratio of the integrated fluorescence intensities of the two solutions (recorded under identical conditions) will yield the ratio of the quantum yield values based on the following equation

$$\Phi_X = \Phi_{ST}\left(\frac{\mathrm{Grad}_X}{\mathrm{Grad}_{ST}}\right)\left(\frac{\eta_X^2}{\eta_{ST}^2}\right), \quad (9)$$

where the subscripts ST and X denote standard and test respectively, Φ is the fluorescence quantum yield, Grad the gradient of integrated fluorescence intensity versus absorbance, and η the refractive index of the solvent used.

1-1.4 Tumor angiogenesis

Tumor angiogenesis is the proliferation of a network of blood vessels that penetrates into cancerous growths, supplying nutrients and oxygen, and removing waste products. This process starts with cancerous tumor cells releasing signaling molecules to surrounding normal host tissue which in turn activates certain genes in the host tissue which make proteins to encourage growth of new blood vessels. Furthermore, the increased demand of oxygen due to the hyper metabolism of tumors reduces the oxygen saturation of the hemoglobin content within the surrounding tissue as seen in **Figure 1-1**. Multi-wavelength optical imaging reveals both angiogenesis and hyper metabolism, both of which are important hallmarks of tumor proliferation, growth, and

metastasis [18-19]. Angiogenesis is considered one of the fastest growing fields in biomedical research, and advances in our basic understanding of this process and its application have been rapid.

Tumor hypoxia leads to an increased level of regulatory transcription factors such as hypoxia inducible factor (HIF-1α) to upregulate the expression of genes associated with tumor initiation, malignant progression, metastasis and resistance to chemotherapy and radiotherapy [20-22,26]. However, the effects of angiogenesis remain controversial. HIF-1α protein expression is similar in normoxic and hypoxic conditions but tends to stabilize in hypoxic environments. HIF-1α combines with HIF-1β and activates several HIF-1 target gene to express proteins, such as VEGF (Vascular endothelial growth factor), which is a significant protein involved in angiogenesis.[24,27] Hence, many studies indicate that most solid tumors, regardless of site of origin, contain hypoxic regions of biological and clinical significance. [25]

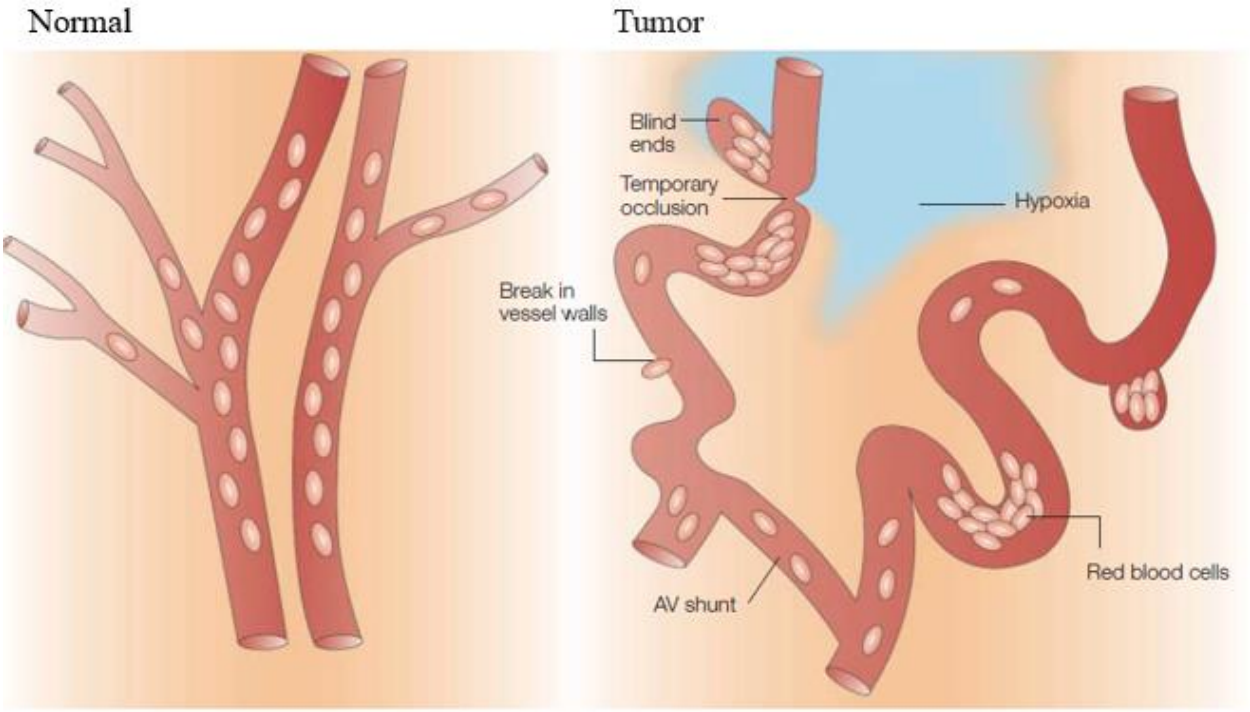

Figure 1-1 The vasculature structural differences of normal and malignant tissues. Normal tissues have relatively uniform and well-ordered blood vessels that are sufficiently close together to oxygenate all of the tissue, blood vessels in tumors are tortuous, have incomplete vessel walls, have sluggish and irregular blood flow, and have regions of hypoxia between the vessels. (Image from **Ref. 20**)

1-1.5 Statement of work

The overarching goal of this research is to increase the optical contrast in PAI and improve tumor hypoxia targeting using fluorescence imaging modality, to enable early detection of cancerous tumors resulting in decrease or morbidity and mortality in patients. This dissertation is structured into two main sections. Chapter 2 introduces the evaluation of several novel porphyrin dyes as PAI contrast agents in direct comparison to the commonly used indocyanine green (ICG) and blood. Imaging of a sub-mm target containing quinoline-annulated porphyrin up to 2 cm depth in a tissue-like matrix exceeds the performance of imaging the similar target containing ICG, which suggests the use of quinoline-annulated porphyrins as potential contrast agents for cancer detection using PAI. Chapter 3 of the dissertation reports an investigation of the unsubstituted imidazole derivative as well as the 4-nitroimidazole ICG-conjugate for targeting tumor hypoxia using fluorescence imaging modality. The performance of 4-nitroimidazole dye has been validated by imaging tumor cells *in vitro* and animals *in vivo* and compared the results with the 2-nitroimidazole dye, using the imidazole derivative as the reference. Histology images of tumor stained sections was performed to confirm hypoxic condition of mice groups.

1-2 References

1. N, H. and e.a. Noone AM, *SEER Cancer Statistics Review*, 1975-2011, 2014, National Cancer Institute. : Bethesda, MD.

2. Peters, V.G., et al., *Optical properties of normal and diseased human breast tissues in the visible and near infrared.* Phys Med Biol, 1990. 35(9): p. 1317-34.

3. Troy, T.L., D.L. Page, and E.M. Sevick-Muraca, *Optical properties of normal and diseased breast tissues: prognosis for optical mammography*. J Biomed Opt, 1996. 1(3): p. 342-55.

4. Mallidi, S., G.P. Luke, and S. Emelianov, *Photoacoustic imaging in cancer detection, diagnosis, and treatment guidance*. Trends Biotechnol, 2011. 29(5): p. 213-21.

5. Hahn, M.A., et al., *Nanoparticles as contrast agents for in-vivo bioimaging: current status and future perspectives.* Anal Bioanal Chem, 2011. 399(1): p. 3-27.

6. Lovell, J.F., et al., *Porphysome nanovesicles generated by porphyrin bilayers for use as multimodal biophotonic contrast agents*. Nat Mater, 2011. 10(4): p. 324-32.

7. Biswal, N.C., et al., *Fluorescence imaging of vascular endothelial growth factor in tumors for mice embedded in a turbid medium*. J Biomed Opt, 2010. 15(1): p. 016012.

8. Kai Licha, B.R., Vasilis Ntziachristos, Andreas Becker, Britton Chance and and W. Semmler, *Hydrophilic Cyanine Dyes as Contrast Agents for Near-infrared Tumor.* Photochemistry and Photobiology, 2000. 72(3): 392–398.

9. Chitneni, S.K., et al., *Molecular imaging of hypoxia*. J Nucl Med, 2011. 52(2): p. 165-8.

10. Achilefu, S., et al., *Novel receptor-targeted fluorescent contrast agents for in vivo tumor imaging*. Invest Radiol, 2000. 35(8): p. 479-85.

11. Rosencwaig A *Photoacoustics and Photoacoustic Spectroscopy* (Chemical Analysis) 1980 (New York: Wiley).

12. Bell AG. *On the production of sound by light*. Am J Sci. 1880; 20(305)

13. Valery Tuchin, *Tissue Optics: Light Scattering Methods and Instruments for Medical Diagnosis*, SPIE Press, 2nd Edition, 2007.

14. A. T. R. Williams, S. A. Winfield and J. N. Miller, *Relative fluorescence quantum yields using a computer controlled luminescence spectrometer*, Analyst, 1983, 108, 1067.

15. Xu, Y., et al., *Targeting tumor hypoxia with 2-nitroimidazole-indocyanine green dye conjugates.* J Biomed Opt, 2013. 18(6): p. 66009.

16. Okuda, K., et al., *2-Nitroimidazole-tricarbocyanine conjugate as a near-infrared fluorescent probe for in vivo imaging of tumor hypoxia.* Bioconjug Chem, 2012. 23(3): p. 324-9.

17. Biswal, N.C., et al., *Imaging tumor hypoxia by near-infrared fluorescence tomography.* J Biomed Opt, 2011. 16(6): p. 066009.

18. L V Wang and H Wu, *Biomedical Optics: Principles and Imaging*, John Wiley and Sons Inc., 2007.

19. P Vaupel, F Kallinowski, P Okunieff P, "*Blood flow, oxygen and nutrient supply, and metabolic microenvironment of human tumors: a review*," Cancer Research 49, pp 6449-6465 (1989).

20. Brown, J. M. & Wilson, W. R. *Exploiting tumour hypoxia in cancer treatment*. Nat. Rev. Cancer 4, 437–447 (2004).

21. Harada, H. *How can we overcome tumor hypoxia in radiation therapy*? J. Radiat. Res. 52, 545–556 (2011).

22. Moeller, B. J., Cao, Y., Li, C. Y. & Dewhirst, M. W. *Radiation activates HIF-1 to regulate vascular radiosensitivity in tumors: role of reoxygenation, free radicals, and stress granules.* Cancer Cell 5, 429–441 (2004).

23. L.V. Wang, "*Tutorial on Photoacoustic Microscopy and Computed Tomography*," IEEE Journal of Selected Topics in Quantum Electronics 14(1), 171-179 (2008).

24. Zeng, Y., Y. Liu, et al. (2015). "*Phosphorescence monitoring of hypoxic microenvironment in solid-tumors to evaluate chemotherapeutic effects using the hypoxia-sensitive iridium (III) coordination compound*." PLoS One 10(3): e0121293.

25. Dhani, N., A. Fyles, et al. (2015). "*The clinical significance of hypoxia in human cancers*." Semin Nucl Med 45(2): 110-121.

26. Zhou, J., T. Schmid, et al. (2006). "*Tumor hypoxia and cancer progression*." Cancer Lett 237(1): 10-21.

27. Wouters, B. G., T. van den Beucken, et al. (2004). "Targeting hypoxia tolerance in cancer." Drug Resist Updat 7(1): 25-40.

Chapter 2

Porphyrin-derived photoacoustic contrast agents

2-1 Introduction

Photoacoustic imaging (PAI) is a non-invasive biomedical imaging modality that combines optical and ultrasound imaging in such a way that its key characteristics are superior to each of the component imaging techniques.[1-4] The absorption of a light pulse by a chromophore causes a rapid and transient rise in temperature (in the order of mK), leading to a localized thermal-elastic expansion. As a laser beam pulsed in the nanosecond range is scanned through an object to be imaged, the emitted ultrasonic wave profile is acquired with standard ultrasonic transducers. The data are used to reconstruct 2D or 3D optical absorption maps. PAI combines the advantages of high optical contrast and ultrasound (sub-mm) spatial resolution.[1, 5-7]

Using the high optical absorption of the endogenous chromophore hemoglobin, PAI proved itself as a powerful tool for imaging the blood content of, for instance, the vascular network of cancers in rodent brains or ovary tissues, in mesoscopic biological objects, or present in whole animals.[8-12] However, to achieve a good signal to noise ratio in reasonably short time that would make PAI of deeply-seated lesions practical, the sensitivity of PAI at greater tissue depths needs to be improved.[5] Furthermore, many cancers, particularly in their early stages, cannot be detected by their intrinsic vascular contrast.[13] These current shortcomings in PAI suggest the use of exogenous contrast agents.

The native light absorption of tissue is wavelength-dependent, with the least absorbance

in the NIR region. For instance, the wavelength of maximum penetration of breast tissue is ~725 nm; whole blood has an absorption minimum at ~710 nm.[14] Thus, using near-infrared wavelengths within the 'spectroscopic window' (~700-1000 nm) allows tissues to be imaged at deeper depth (several cm) than most other optical imaging techniques. It thus follows that a good PAI contrast agent ought to have a strong absorption in NIR, particular in the region between ~700 and 800 nm. Currently, the maximum photoacoustic imaging depth of 8.4 cm have been achieved in chicken breast tissue.[47] Internal light delivery has also been proposed to image organs beneath the skin.[48] Recently, a dual-modality photoacoustic and ultrasonic imaging system to noninvasively detect sentinel lymph nodes based on the accumulation of methylene blue dye has been developed.[49] Zackrisson, et al. reviewed the recent advances of photoacoustic imaging in biomedical research, and discussed of strategies for clinical translation of the PAI technique. Including its use as a noninvasive imaging of the breast, sentinel lymph nodes, skin, thyroid, eye, prostate, and ovaries (transvaginal); minimally invasive endoscopic imaging of gastrointestinal tract, bladder, and circulating tumor cells (*in vivo* flow cytometry); and intraoperative imaging for assessment of tumor margins and metastases.[50]

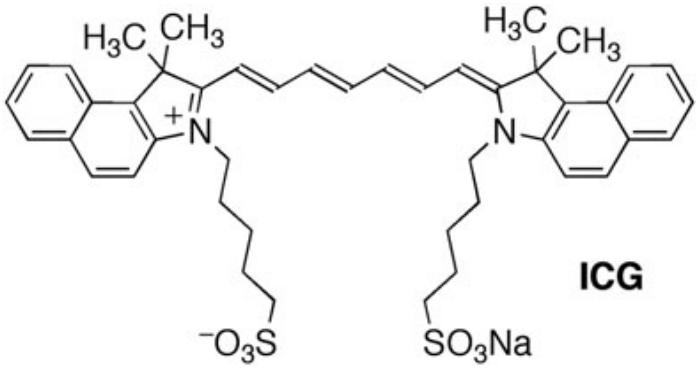

The FDA-approved ocular angiographic dye indocyanine green (ICG) and ICG

derivatives fulfill this spectroscopic requirement.[15] ICG is confined to the vasculature space and it clears rapidly (t1/2 < 3 min), complicating longitudinal *in vivo* studies. This lead to the development of other contrast agents, such as metal-based nanoparticles combined with and without organic dyes, nanotubes, and porphyrin-based liposomes.[16-34] Water-soluble polydopamine and linear melanin have also been tested as contrast agent for photoacoustic imaging with an imaging depth of 12 mm.[51] Since the safety of the use of nanoparticles in medicine is unclear so far,[35] it led to the search for novel ways to, for instance, generate dyes in tissue.[7, 36, 37] For instance, photoacoustic probes activatable by cancer markers were developed.[38, 52] Notably rare from all these reports are novel small molecular dyes as PAI contrast agents.[39, 40]

2-2 Methods and Procedures

2-2.1 Materials

The group of Prof. Christian Brueckner in the Department of Chemistry at the University of Connecticut has synthesized six free base tetrapyrrolicchromophores, three of which are quinoline-annulated porphyrins dyes 1 through 3 prepared from TPP as described in the literature,[41] and three morpholinobacteriochlorins dyes 4 through 6 (listed in **Figure 2-1**) were also prepared from TPP as described.[42] These agents exhibit a broad optical absorption profiles in the near-infrared window (~700-850 nm) and possess, in comparison to regular porphyrins, unusually low fluorescence emission and $^1O_2$ quantum yields. ICG was purchased from Sigma Aldrich. The dyes 1 through 3 and ICG were also tested in an aqueous solution using the FDA-approved excipient Cremophore EL®, at A = 1.0 at the wavelengths listed in **Table 2-2** at 1 cm and 2 cm path lengths).. The dyes 1 through 6 and ICG were also dissolved in DMF at a

concentration so that they possessed all identical absorbances (A = 1.0 at the wavelengths listed in **Table 2-3** at 1 cm and 2 cm path lengths).

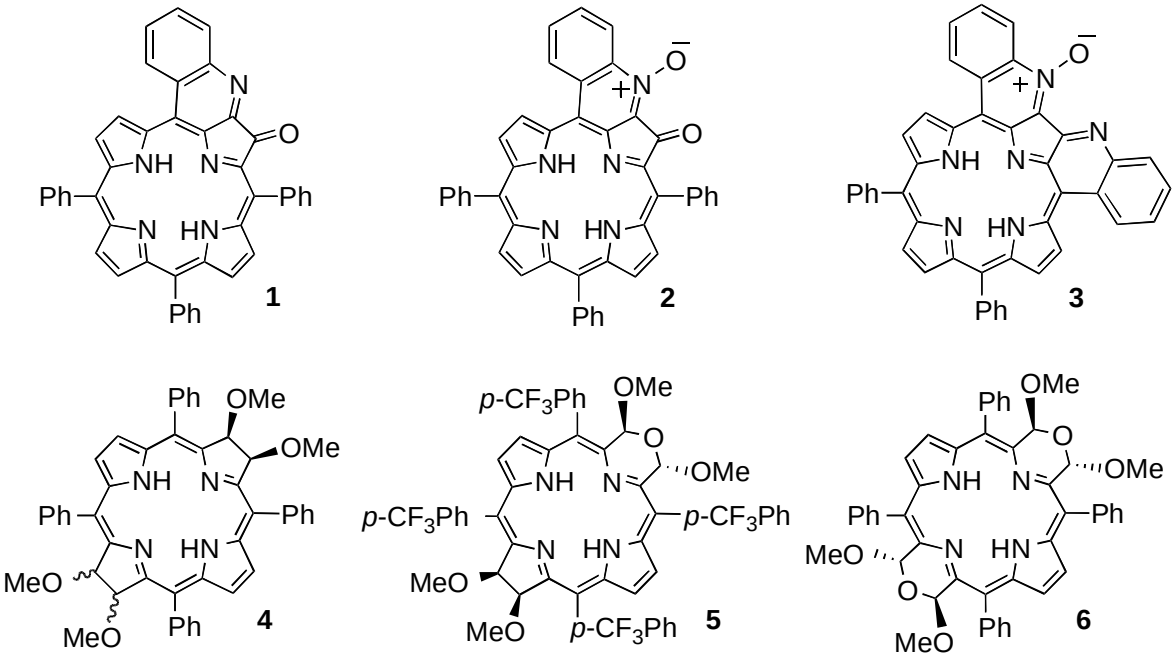

Figure 2-1 Structures of the NIR chromophores investigated.

The UV-Vis absorption spectra for all compounds 1 through 6 shown in **Figure 2-2** were recorded using a Cary 50 spectrophotometer (Varian Analytical Instruments, Walnut Creek, CA). The reported results indicate a strong optical absorbance wavelengths between 700 and 900 nm.

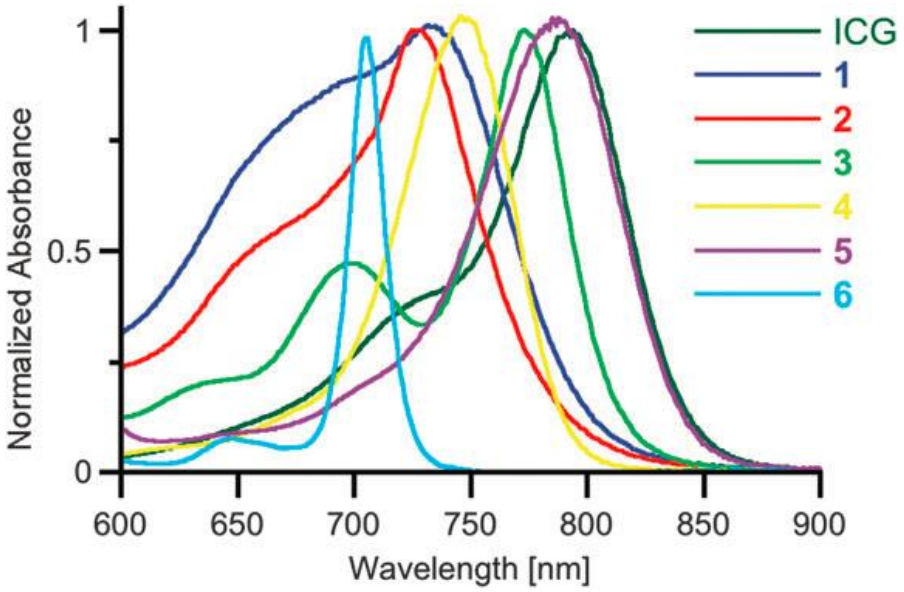

Figure 2-2 UV-Vis spectra of the chromophores in DMF used in the PAI experiments. The concentrations were adjusted to an absorption value of 1.0 ±0.05 at the respective λ_{max} wavelength, 1 cm glass cuvette.

The photophysical properties are associated with the molecule energy behavior upon absorption of light. The molecular absorbance and emission of light was first described by Aleksander Jablonski. In his diagram he explains how electrons are excited from the ground state into higher electronic energy states called singlet states, and the events that occur as these excited molecules relax by photon emission and other mechanisms to eventually fall back into the ground-level energy state. As you can see in **Figure 2-3**, excited states are short-term, so the relaxation back to the ground state happens through emitting fluorescence or thermally emitting light quanta through internal conversion (IC). Another possibility that an electron undergo an intersystem crossing ISC process transitioning from a singlet state to a triplet state, the relaxation from an excited triplet state to the ground singlet state, is either through phosphorescence or, through interaction with triplet oxygen ($^3\Sigma_g$), generating singlet oxygen ($^1\Delta_g$).

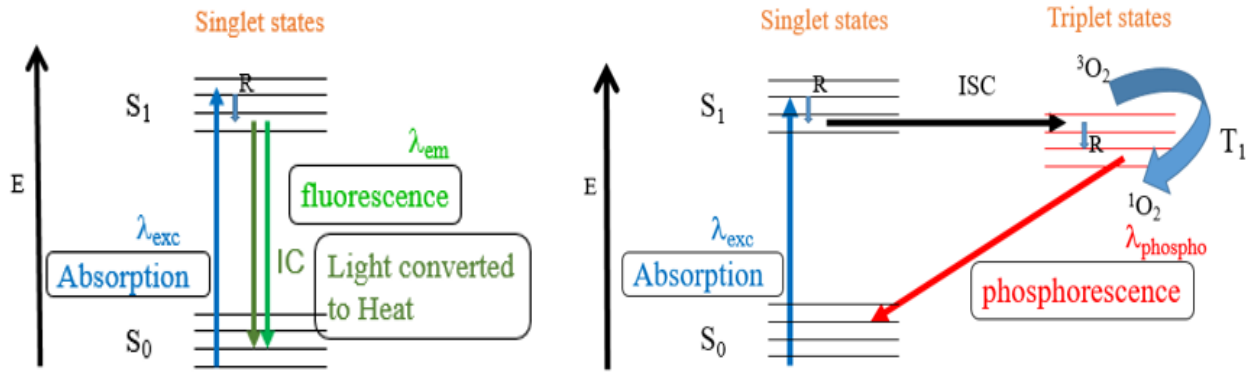

Figure 2-3 Jablonski diagram: When a molecule absorbs light, it undergo a transition into an excited singlet state, from there the system either relaxes back to the ground state through fluorescence or thermally through internal conversion (IC). It can also undergo an inter-system crossing (ISC) into an excited triplet state where it relaxes either thermally, through phosphorescence or through interaction with triplet oxygen, generating a singlet oxygen.

Thus, the photophysical parameters such as singlet state lifetime (τ_{S1}), the fluorescence quantum yield (Φ_{Fluo}), the ISC quantum yield (Φ_{ISC}), and the singlet oxygen quantum yield (Φ_{Δ}) are crucial parameters to assess the relaxation pathways of the chromophores investigated. Some of the photophysical properties in **Table 2-1** were recorded in collaboration with A. Vollertsen, as part of his MS Thesis, Humboldt-University, Berlin, 2012.

Table 2-1 Photophysical properties of the dyes investigated

	λ_{max}/nm	log ε at λ_{max}/ $cm^{-1}M^{-1}$	Φ_{Fluo}/%	Φ_{ISC}/% (± 3%)	Φ_{Δ}/%[n] (± 10%)	τ_{S_1}/ns (± 10%)
ICG	776,[d] 794[j]	5.06	8[g]	0.6[h]	–[i]	0.15[h]
TPP[a]	648	3.61	9 (11)[c]	50	45	0.24
1[k]	728	4.30	< 1	2	5	0.04
2[k]	726	4.49	< 1	b.d.[e]	< 1	b.d.[e]
3[m]	773	4.44	0.004	–[b]	4[o]	0.74, 1.70[f]
7[k,j]	667	3.75	< 1	27	7	1.33
4[k,j]	704	4.71	17	45	40	5.40
5[k,j,l]	745	4.54	3	85	–[b]	3.77
6[k,j]	790	4.36	0.01	87	12	0.45

[a]In toluene.[b]Not determined. [c] G. H. Barnett, M. F. Hudson, and K. M. Smith, *J. Chem. Soc. Perkin Trans. I,* 1975, 1401-1403.[d]At 6.5 µM ICG in H_2O, M. L. J. Landsman, G. Kwant, G. A. Mook, W. G. Zijlstra, *J. Appl. Physiol.*, 1976, 40, 575–583. [e]Below the detection limit. [f] Biexponential decay. [g] J. Pauli, R. Brehm, M. Spieles, W. A. Kaiser, I. Hilger, and U. Resch-Genger*J. Fluoresc.*, 2010, 20, 681–693. [h]In O_2-free H_2O. T. Luo, MSc Thesis, University of Waterloo, 2008. [i]While ICG does not appear to generate much, if any, $^1O_2$ upon radiation, it generates medicinally relevant reactive oxygen species: S. Fickweiler, R.-M. Szeimies, W. Bäumler, P Steinbach, S. Karrer, A. E. Goetz, C. Abels, and F. Hofstädter, *J. Photochem. Photobiol. B*, 1997, 38, 178–183.[j]Ref. 22. [k]λ_{max} and log ε in CH_2Cl_2, all else in DMF. [l] Data for the closely related *meso*-tetraphenyl derivative. [m]λ_{max} and log ε in CH_2Cl_2, all else in DMSO. [n]$\lambda_{excitation} = \lambda_{Soret}$. [o] At $\lambda_{excitation}$ = 625 nm, Φ_{Δ} = 21%, a finding rationalized by the presence of non-sensitizing dimers that are excited at λ_{Soret}

2-2.2 Photoacoustic System Description

The PAI system has been designed in our laboratory, which allows connection of any type of ultrasound transducer array with a maximum of 64 elements and center frequency scalable with the central frequency and bandwidth of the ultrasound transducer between 1 and 10 MHz. The two receiving units of 32-channels each amplify channel data independently by 20 dB before 32:1 multiplexing. Then, the outputs of the two multiplexers are further amplified by two independent two-stage variable gain amplifiers and filtered with 0.5-10 MHz band pass filters. The total gain of the system is typically set to 60 dB. The achieved imaging speed of this system

in PA mode is 5 frames per second. The system utilizes a unique field programmable gate array (FPGA) based reconfigurable processor that allows real-time switching and interlacing between the two imaging modalities (i.e. ultrasound and photoacoustic imaging).The system features a modular design and the ability of real-time parallel acquisition from 64 channels with each channel sampled at 40MHz.[43]

Photoacoustic images were reconstructed using a typical delay and sum algorithm based on the transducer array geometry. These images were then plotted using a color scale. A tunable Ti-Sapphire laser (Symphotics TII, LS-2134; Symphotics, Camarillo, CA), optically pumped with a Q-switched Nd:YAG laser (Symphotics-TII, LS-2122), operating in the spectral range of 700nm-1000 nm, was used to illuminate the tubing target with an average power of radiant exposure of 18 $mJxcm^{-2}$, i.e., well below the ANSI limits of 21 $mJxcm^{-2}$, for the shortest wavelengths used.[44] The optical wavelengths used for each dye based on the peak value of the UV-Vis absorption data are given in **Table 2-3**.

2-2.3 Photoacoustic Phantom Studies

The feasibility of the porphyrins to serve as PAT contrast agents was tested first using a co-registering ultrasound and photoacoustic imaging system. Tubing was imaged while injecting different porphyrin-based and benchmark (ICG) contrast agents. An Nd:YAG laser set at 745 nm, 19.0 mW power to illuminate the samples was used. Photoacoustic measurements were taken for each sample with a single element ultrasound transducer connected to a Panametrics 5073PR for amplification and filtering. The dyes have shown enhanced photoacoustic measurement over the ICG benchmark used. The monoquinoline-fused dye 3 diluted at 500

micro Molar was first used which resulted in 3.7 v signal power, and the bis-quinoline-fused N-oxide dye 1 diluted at 400 micro Molar resulted in 3.8 v signal power while ICG resulted in 2.02 v signal power under the same measurement conditions. These results encouraged us to further evaluate the PAI signal strengths and compare them to blood and ICG.

The phantom studies to evaluate the dyes relative to ICG were performed using the set-up shown in **Figure 2-4**. A translucent polyethylene tube with an inner diameter of 0.38 mm and outer diameter of 1.09 mm was filled with the standard solutions of the dyes 1 through 6, ICG and day-old whole rat blood using a manual syringe. The tube was immersed at 1 and 2 cm depths in a tank filled with a 4% intralipid suspension (absorption coefficient $\mu a = 0.01\ cm^{-1}$, reduced scattering coefficient $\mu s' = 4\ cm^{-1}$.[45] Both ends of the tubing comes out of the tank.

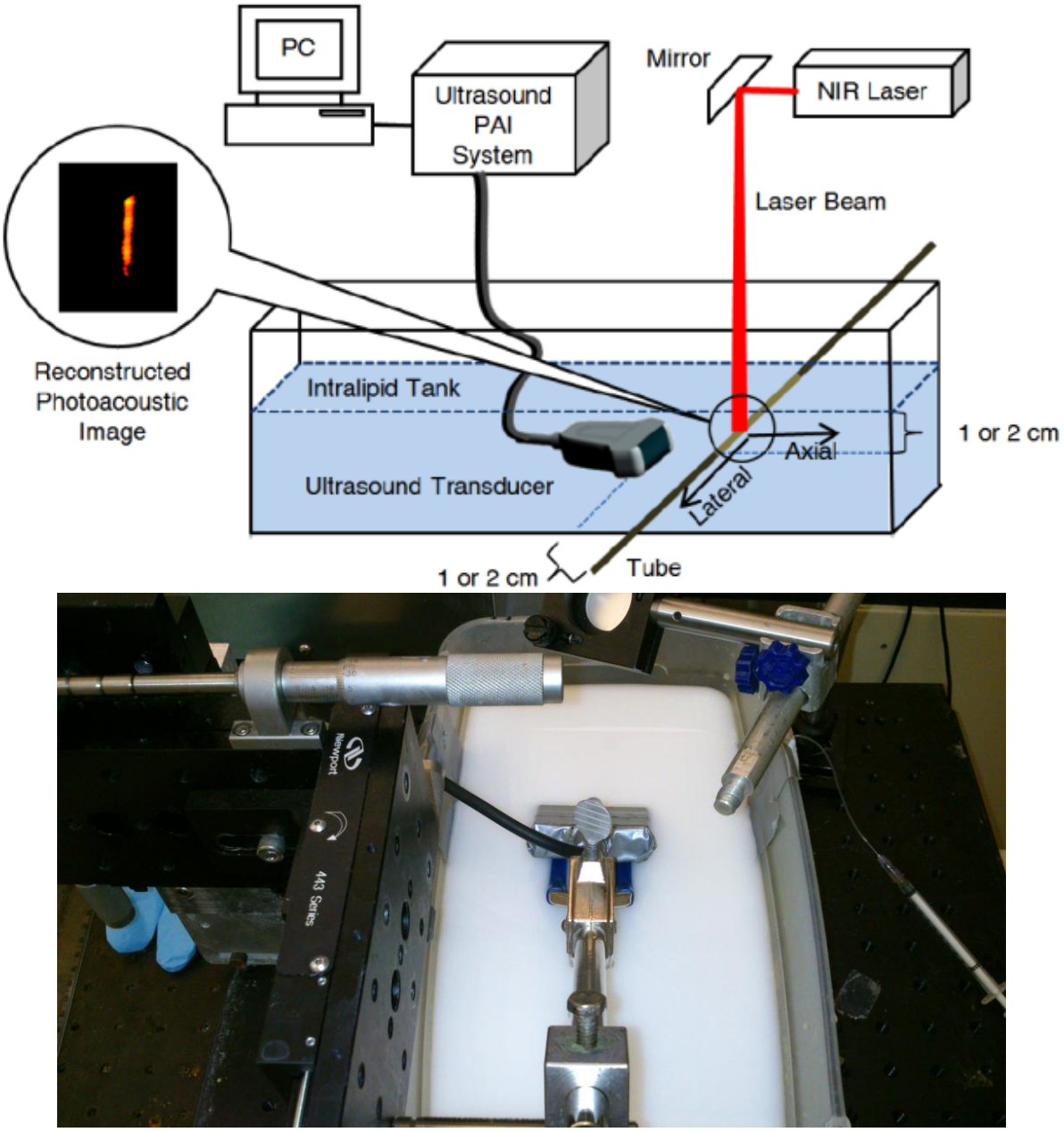

Figure 2-4 PAI experimental setup. Details: Nd:YAG-pumped tunable Ti:Sapphire laser, average power of 18 mJ×cm^{-2}; ultrasound transducer of central frequency 1.3 MHz and bandwidth of 80%, connected to a 64 channel ultrasound PAI system.

Porphyrin solutions were injected one by one into the tubing and tested, after every measurement the tube will be flushed with alcohol twice followed by each injection. The

samples are then recollected from the other end of the tube. A different syringe was used for each dye to avoid contamination. Upon illumination with an NIR laser tuned to the λ_{max} of the dye investigated (**Table 2-3**) and spread to 2 cm diameter width at the point where it intersected with the tube. The photoacoustic measurements were recorded for each sample solution using a commercial low-frequency transducer array (produced by Vermon, France), and consisted of 64 elements with 0.85 mm pitch. The center frequency of the transducer was 1.3 MHz and bandwidth of 80%, connected to a 64 channel ultrasound PAI system. The array was held at 1 and 2 cm, respectively, away from the center of the intersection of the NIR beam and the tube. The signal was then collected and processed by the PAI system. Photoacoustic images were reconstructed using a typical ultrasound beam forming algorithm based on the transducer array geometry.

2-3 Results and Discussion

Chromophores 1 through 6 were selected for this investigation because of their UV-Vis NIR absorption properties. Their λ_{max} values (the wavelengths of the band of longest absorption) in DMF between 726 nm and 790 nm fall into the spectroscopic window of tissue, and all fall within a range of 70 nm of those of ICG in the same solvent as seen in the graph in **Figure 2-2**, allowing for a meaningful direct comparison of the PAI data accrued. Upon light absorption, porphyrins generally undergo a $\pi \rightarrow \pi^*$ transition into an excited singlet state. From there the system either relaxes back to the ground state through fluorescence or thermally through internal conversion (IC). It can also undergo an inter-system crossing (ISC) into an excited triplet state. In turn, the triplet state relaxes either thermally, through phosphorescence or, frequently

observed in porphyrins, through interaction with triplet oxygen ($^3\Sigma_g$), generating singlet oxygen ($^1\Delta_g$). Thus, the singlet state lifetime (τ_{S1}), the fluorescence quantum yield (Φ_{Fluo}), the ISC quantum yield (Φ_{ISC}), and the singlet oxygen quantum yield (Φ_{Δ}) are crucial parameters to assess the relaxation pathways of the chromophores investigated.

Two series of experiments were performed. In one, solutions of the dyes 1 through 3 and ICG in PBS/1% DMF/1% Cremophore EL® were prepared at concentrations that resulted all solutions to possess an equal absorption at λ_{max} (O.D. of 1.0 at 1 cm path length, see **Figure 2-2**), and was irradiated at λ_{max}. Since all solutions absorbed within a narrow window, the energy input difference between the extremes of λ_{max} is less than 9%. Empirically, the data of the PAI experiments was found to vary upon replication by up to 7%, i.e. the simplification of using different irradiation wavelengths/energies at equal absorbance values is within acceptable limits. The phantom studies described below were performed, the results of which are listed in **Table 2-2**.

Table 2-2 Comparison of the PAI signal strengths in the phantom study

	$\lambda_{irradiation}$/nm	Relative PAI signal strength at 1 cm depth	Relative PAI signal strength at 2 cm depth
ICG	790	1.0	1.0
1	765	1.6	1.5
2	755	1.4	1.4
3	780	1.0	1.1

To allow a much better direct comparison of the PAI signal strength generated by ICG, a blood sample and any given dye, and to allow a correlation to the photophysical data

measured primarily in DMF (**Table 2-1**), a second series of experiments was set up. The spectra of the dyes 1 through 6 all overlap with the spectrum of ICG. Thus, DMF solutions of the dyes and ICG were prepared and the isoabsorbance point for each dye-ICG pair was determined. Then, the concentration of the solutions was adjusted to an O.D. of 1.0 at the isoabsorbance wavelength (at 1 cm path length; see **Table 2-3** for the $\lambda_{irradiation}$ used), thus assuring that each ICG-dye pair would receive the identical energy input upon irradiation at this wavelength. The blood sample was used as is and irradiated at 750 nm, an arbitrary wavelength in the middle of the range of the $\lambda_{irradiation}$ used.

The phantom studies to evaluate the dyes relative to ICG were performed using the set-up shown in **Figure 2-4**. A translucent polyethylene tube with an inner diameter of 0.38 mm was filled with the standard DMF solutions of the dyes 1 through 6 and ICG. The tube was immersed at 1 and 2 cm depths in a tank filled with a 4% intralipid suspension, a white opaque emulsion of soy bean oil, egg phospholipids and glycerin. This emulsion is widely used to simulate the scattering properties of biological tissues at wavelengths in the red and infrared ranges, where tissue is highly scattering but has a rather low absorption coefficient.[45]

Upon illumination with a NIR laser tuned to the $\lambda_{irradiation}$ chosen and spread to 2 cm diameter width at the point it intersected with the tube, the photoacoustic measurements were recorded for each sample solution using a commercial low-frequency transducer array. The array was held at a fixed position 1 cm and 2 cm away from the center of the intersection of the NIR beam and the tube, respectively. The PA signal was collected and processed by a PAI system. Photoacoustic images were reconstructed using a typical ultrasound beam-forming algorithm

based on the transducer array geometry. The data thus obtained were plotted using a color scale, providing the photoacoustic images shown in **Figure 2-5**. The PAI signal strengths relative to those obtained for ICG in the same solvents are listed in **Table 2-3**.

Table 2-3 Comparison of the PAI signal strengths in the phantom study for dyes 1-6 in solvent DMF

	$\lambda_{irradiation}$/nm	Relative PAI signal strength at 1 cm depth	Relative PAI signal strength at 2 cm depth
ICG	790	1.0	1.0
blood	750	1.1	1.0
1	765	2.5	2.4
2	755	1.9	1.2
3	780	1.7	1.1
4	715	Below detection	Below detection
5	765	0.5	0.5
6	741	0.8	0.7

At 1 cm depth/detector distance, all dyes tested provide a clear image of the target. However, the intensity of the signal varied. The signal strengths recorded for the quinoline-annulated porphyrin 1 through 3 are 1.7 to 2.5-fold stronger than the signal for the benchmark compound ICG or the blood sample (that showed very similar PAI signal strengths to those obtained with ICG) with compound 1 providing the best signal. The signal strength recorded for dye 1 is still nearly 2.4-fold stronger at 2 cm immersion depth/detector distance, though the relative advantages of these dyes in DMF over ICG are largely eroded. A comparison of the photophysical data for the dyes **(Table 2-1)** with the PAI data in **(Table 2-3)** reveals that the best PAI contrast agent 1 is mostly differentiated from the other two structurally similar compounds (and ICG) by possessing the shortest singlet state lifetime, suggesting that this may have been the

crucial factor for its relatively high efficacy.[46] Using an aqueous solvent for the comparison of the three dyes with ICG, the absolute signal strength and the relative signal strength advantages of the dyes 1 through 3 are not as strong. Given the lower heat capacity of DMF (1.88 $JK^{-1}cm^{-3}$) compared to that of water (4.19 $JK^{-1}cm^{-3}$) (and ignoring factors such as their varying thermal pressure coefficients),[46] the lower light absorption-induced photoacoustic pressure in water does not surprise. The fact, however, that the relative drop of the signal strengths with phanton immersion depth/detector distance is not as steep when using the aqueous solvent versus DMF, does not find a simple explanation.

As a result of the higher signal-to-noise ratios, the PAI images recorded with dyes 1 and 2 also show a better-defined tubing structure than the image recorded with ICG (**Figure 2-5)**; note that the images shown were recorded using aqueous solvents. The signal strength recorded for 3 (no image shown) was identical to that recorded for ICG. However, the ~4-fold higher absorptivity of ICG compared to the porphyrinoids at around 750 nm suggest that ICG is still a better contrast agent at equal concentrations. As it could be predicted based on their higher fluorescence quantum yields, larger ISC yields, longer-lived excited singlet states, and higher singlet oxygen quantum yields, the bacteriochlorins 4 through 6 did not perform as well as the quinoline-annulated porphyrins or ICG in the PAI experiments. This illustrates well the need to fine-tune all photophysical properties of a potential PAI imaging dye, not just their optimal absorption properties.

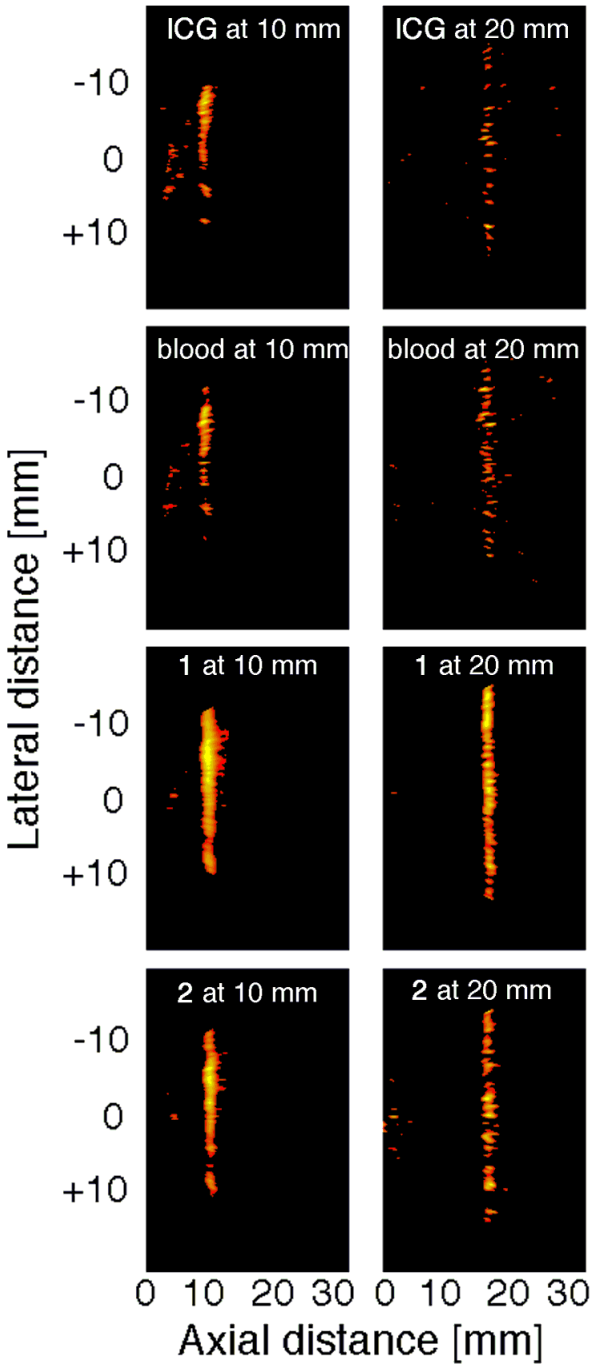

Figure 2-5 Photoacoustic images of the dyes indicated, dissolved in an aqueous solution containing the surfactant Cremophore EL to a concentration resulting in an absorbance value of A = 1.0 at 1 cm path lengths. Left column: Targets located at 1 cm depths, right column targets locates at 2 cm depths. Targets: a transparent polyethylene tube of inner diameter 0.38 mm and outer diameter 1.09 mm filled with the dye solution, submersed in an opaque 4% Intralipid suspension. To best visualize the contrast, the dynamic range of the display was set to 10 dB.

2-4 Summary

Direct comparison was performed for a range of porphyrinoids with NIR absorbing properties belonging to two different compound classes (quinoline-annulated porphyrins and bacteriochlorins) as exogenous PAI imaging contrast agents in phantom studies. Also demonstrated the imaging of a sub-mm target at up to 2 cm depth in a tissue-like matrix whereby some porphyrinoids matched or exceeded the performance of the benchmark dye ICG at equal absorbance or the performance of pure blood. This suggests the use of quinoline-annulated porphyrins as potential contrast agents for *in vivo* use for multi-cm deep tissue PAI. While this data does not allow any obvious direct correlations between the photophysical data and the PAI contrast enhancement measured to be made, the need for the ability of the dyes to access a very efficient thermal relaxation pathway is once again highlighted. Moreover, more members of NIR-absorbing porphyrinoids are being screened using a simple and rapid screening tool such as the one used here, a direct correlation between the PAI signal strength and key photophysical parameters may come into focus, further assisting in the design of optimized contrast agents. The best contrast agents identified in this study, the two quinoline-annulated porphyrins, are currently undergoing a range of *in cyto* and *in vivo* cytotoxicity and PAI studies.

2-5 References

1. Kim, C., C. Favazza, and L.V. Wang, *In vivo photoacoustic tomography of chemicals: high-resolution functional and molecular optical imaging at new depths.* Chem Rev, 2010. 110(5): p. 2756-82.

2. Pysz, M.A., S.S. Gambhir, and J.K. Willmann, *Molecular imaging: current status and emerging strategies.* Clin Radiol, 2010. 65(7): p. 500-16.

3. Levi, J., et al., *Design, synthesis, and imaging of an activatable photoacoustic probe.* J Am Chem Soc, 2010. 132(32): p. 11264-9.

4. Xu, M. and L.V. Wang, *Photoacoustic imaging in biomedicine.* Review of Scientific Instruments, 2006. 77(4): p. 041101.

5. Esenaliev, R.O., A.A. Karabutov, and A.A. Oraevsky, *Sensitivity of laser optoacoustic imaging in detection of small deeply embedded tumors.* IEEE J. Sel. Top. Quantum Electron., 1999. 5: p. 981-988.

6. Kruger, R.A., D.R. Reinecke, and G.A. Kruger, *Thermoacoustic computed tomography technical considerations.* Med. Phys., 1999. 26: p. 1832-1837.

7. Stender, A.S., et al., *Single Cell Optical Imaging and Spectroscopy.* Chem. Rev., 2013. 113(4): p. 2469–2527.

8. Aguirre, A., et al., *Coregistered three-dimensional ultrasound and photoacoustic imaging system for ovarian tissue characterization.* J Biomed Opt, 2009. 14(5): p. 054014.

9. Wang, X.D., et al., *Noninvasive laser-induced photoacoustic tomography for structural and functional in vivo imaging of the brain.* Nature Biotechnol., 2003. 21: p. 803-806.

10. Holen, C.G.A., et al., *Three-dimensional photoacoustic imaging of blood vessels in tissue.* Optics Lett., 1998. 23: p. 648-650.

11. Ma, R., et al., *Multispectral optoacoustic tomography (MSOT) scanner for whole-body small animal imaging.* Optics Express, 2009. 17(24): p. 21414–21426.

12. Razansky1, D., C. Vinegoni, and V. Ntziachristos, *Imaging of mesoscopic-scale organisms using selective-plane optoacoustic tomography.* Phys. Med. Biol., 2009. 54: p. 2769-2777.

13. Troy, T.L., D.L. Page, and E.M. Sevick-Muraca, *Optical properties of normal and diseased breast tissues: prognosis for optical mammography.* J Biomed Opt, 1996. 1(3): p. 342-55.

14. Cerussi, A.E., et al., *Sources of Absorption and Scattering Contrast for Near-Infrared Optical Mammography.* Acad Radiol, 2001. 8(3): p. 211-218.

15. Luo, S., et al., *A review of NIR dyes in cancer targeting and imaging.* Biomaterials, 2011. 32(29): p. 7127-38.

16. De La Zerda, A., et al., *Carbon nanotubes as photoacoustic molecular imaging agents in living mice.* Nature Nanotechnol., 2008. 3(9): p. 557-562.

17. Song, K.H., et al., *Near-Infrared Gold Nanocages as a New Class of Tracers for Photoacoustic Sentinel Lymph Node Mapping on a Rat Model.* Nano Letters, 2008. 9(1): p. 183-188.

18. Yang, X., et al., *Photoacoustic tomography with novel optical contrast agents based on gold nanoparticles containing near-infrared dyes.* Proc. SPIE 2008. 6856: p. 6856601.

19. Wang, B., et al., *Plasmonic Intravascular Photoacoustic Imaging for Detection of Macrophages in Atherosclerotic Plaques.* Nano Lett., 2008. 9(6): p. 2212-2217.

20. Mallidi, S., et al., *Multiwavelength Photoacoustic Imaging and Plasmon Resonance Coupling of Gold Nanoparticles for Selective Detection of Cancer.* Nano Lett., 2009. 9(8): p. 2825-2831.

21. Pan, D., et al., *Molecular Photoacoustic Tomography with Colloidal Nanobeacons.* Angew. Chem. Int.Ed., 2009. 48(23): p. 4170-4173.

22. Yang, X., et al., *Nanoparticles for photoacoustic imaging.* WIREs Nanomed. Nanobiotech., 2009. 1: p. 260-368.

23. Chen, J., et al., *Gold Nanocages: A Novel Class of Multifunctional Nanomaterials for Theranostic Applications.* Advanced Functional Materials, 2010. 20(21): p. 3684-3694.

24. Zerda, A.d.l., et al., *Ultrahigh Sensitivity Carbon Nanotube Agents for Photoacoustic Molecular Imaging in Living Mice.* Nano Lett., 2010. 10(6): p. 2168-2172.

25. Kim, C., C. Favazza, and L.V. Wang, *In Vivo Photoacoustic Tomography of Chemicals: High-Resolution Functional and Molecular Optical Imaging at New Depths.* Chem. Rev., 2010. 110(5): p. 2756-2782.

26. Lovell, J.F., et al., *Porphysome nanovesicles generated by porphyrin bilayers for use as multimodal biophotonic contrast agents.* Nature Mat., 2011. 10: p. 324–332.

27. Moon, G.D., et al., *A New Theranostic System Based on Gold Nanocages and Phase-Change Materials with Unique Features for Photoacoustic Imaging and Controlled Release.* J. Am. Chem. Soc., 2011. 133(13): p. 4762-4765.

28. Pan, D., et al., *Photoacoustic Sentinel Lymph Node Imaging with Self-Assembled Copper Neodecanoate Nanoparticles.* ACS Nano, 2012. 6(2): p. 1260-1267.

29. Jokerst, J.V., et al., *Gold Nanorods for Ovarian Cancer Detection with Photoacoustic Imaging and Resection Guidance via Raman Imaging in Living Mice.* ACS Nano, 2012. 6(11): p. 10366-10377.

30. Ku, G., et al., *Copper Sulfide Nanoparticles As a New Class of Photoacoustic Contrast Agent for Deep Tissue Imaging at 1064 nm.* ACS Nano, 2012. 6(8): p. 7489-7496.

31. Jokerst, J.V., et al., *Photoacoustic Imaging of Mesenchymal Stem Cells in Living Mice via Silica-Coated Gold Nanorods.* ACS Nano, 2012. 6(7): p. 5920-5930.

32. de la Zerda, A., et al., *Family of Enhanced Photoacoustic Imaging Agents for High-Sensitivity and Multiplexing Studies in Living Mice.* ACS Nano, 2012. 6(6): p. 4694-4701.

33. Homan, K.A., et al., *Silver Nanoplate Contrast Agents for in Vivo Molecular Photoacoustic Imaging.* ACS Nano, 2012. 6(1): p. 641-650.

34. Cook, J.R., W. Frey, and S. Emelianov, *Quantitative Photoacoustic Imaging of Nanoparticles in Cells and Tissues.* ACS Nano, 2013. 7(2): p. 1272-1280.

35. Heister, E., et al., *Are Carbon Nanotubes a Natural Solution? Applications in Biology and Medicine.* ACS Appl. Mater. Interfaces, 2013. 5(6): p. 1870-1891.

36. Filonov, G.S., et al., *Deep-Tissue Photoacoustic Tomography of a Genetically Encoded Near-Infrared Fluorescent Probe.* Angew. Chem. Int. Ed., 2011. 51(6): p. 1448-1451.

37. Zhang, Y., et al., *Noninvasive Photoacoustic Microscopy of Living Cells in Two and Three Dimensions through Enhancement by a Metabolite Dye.* Angew. Chem. Int. Ed., 2011. 50(32): p. 7359-7363.

38. Levi, J., et al., *Design, Synthesis, and Imaging of an Activatable Photoacoustic Probe.* J. Am. Chem. Soc., 2010. 132(32): p. 11264-11269.

39. Schaberle, F.A., et al., *Infrared absorbing dyes tailored for detection and therapy of solid tumors.* Proc. SPIE, 2010. 7376: p. 7376X-1–7376X-7

40. Schaberle, F.A., et al., *Multi-specral photoacoustic mapping of bacteriochlorins diffusing through the skin: exploring a new PAT contrast agent.* Proc. SPIE, 2011. 8089: p. 8089Q-1–8089Q-8

41. Joshua Akhigbe, M.Z., ‡ and Christian Br€uckner*,†, *quinoline-annulated prophyrins_Akhigbe.pdf.* ORGANIC LETTERS, 2010. 13(6): p. 1322-1325.

42. Samankumara, L.P., et al., *Syntheses, structures, modification, and optical properties of meso-tetraaryl-2,3-dimethoxychlorin, and two isomeric meso-tetraaryl-2,3,12,13-tetrahydroxybacteriochlorins.* Org Biomol Chem, 2010. 8(8): p. 1951-65.

43. Alqasemi, U., et al., *FPGA-based reconfigurable processor for ultrafast interlaced ultrasound and photoacoustic imaging.* IEEE Trans Ultrason Ferroelectr Freq Control, 2012. 59(7): p. 1344-53.

44. ANSI Z136.1-2007: American National Standard for Safe Use of Lasers, American National Standards Institute Inc. 2007.

45. I. Driver, J.W. Feather, P.R. King, J.B. Dawson Phys. Med. Biol. 1989, 34, 1927–1930.

46. Arnaut, L.G., et al., *Recent advances in photoacoustic calorimetry: Theoretical basis and improvements in experimental design.* Rev. Sci. Instrum., 1992. 63(11): p. 5381–5389.

47. Favazza C, Jassim O, Wang LV, Cornelius L. *In vivo photoacoustic microscopy of human skin. Journal of Investigative Dermatology*. 2010 Apr.130:S145.

48. Bell, MAL.; Guo, X.; Song, DY.; Boctor, EM. Photons Plus Ultrasound: Imaging and Sensing 2014. *Photoacoustic imaging of prostate brachytherapy seeds with transurethral light delivery*; p. 89430N-89430N-6.

49. Garcia-Uribe, A., T. N. Erpelding, et al. (2015). "*Dual-Modality Photoacoustic and Ultrasound Imaging System for Noninvasive Sentinel Lymph Node Detection in Patients with Breast Cancer*." Sci Rep 5: 15748.

50. Zackrisson, S., S. M. van de Ven, et al. (2014). "*Light in and sound out: emerging translational strategies for photoacoustic imaging.*" Cancer Res 74(4): 979-1004.

51. Repenko, T., S. Fokong, et al. (2015). "*Water-soluble dopamine-based polymers for photoacoustic imaging.*" Chem Commun (Camb) 51(28): 6084-6087.

52. Sano, K., M. Ohashi, et al. (2015). "*In vivo photoacoustic imaging of cancer using indocyanine green-labeled monoclonal antibody targeting the epidermal growth factor receptor*." Biochem Biophys Res Commun 464(3): 820-825.

Chapter 3

Dicarboxylic Acid ICG Derivatives Fluorescence Contrast agents

3-1 Introduction

Tumor hypoxia, defined as an oxygen-deprived condition, has been characterized as having detrimental effects on treatment resistance. Hypoxia is a characteristic feature in most solid tumors due to the imbalance between new blood vessel formation and rapid proliferation of cancer cells. [1-3] The interest in tumor hypoxia has been recognized for more than 60 years.[4] Several factors contribute to inadequate oxygen transport and hypoxia, including low vessel density and increased oxygen consumption. Angiogenesis promoted by the tissue itself emerges as a strategy to meet oxygen demand. However, tumor growth often exceeds the capacity of accompanying blood vasculature to deliver adequate quantities of oxygen to the growing cell mass.[5-6,41] The development of effective hypoxia probes can help visualize the tumor development and would impact the current strategies for early tumor detection and diagnosis in improving the outcome of cancer treatment. Additionally, the ability to non-invasively image the early events of tumors will enable the tracking of tumor progression and metastases.[7-16,42] That is of significant value, specially that this phenomenon begins to emerge when the diameter of solid tumor reaches 0.35 mm.[2,40] However, *in vivo* imaging of the early development of tumor remains a great challenge due to the limitations in the sensitivity of current molecular imaging probes, delivery of the probes and the interference of intrinsic background signals.[17-19]

A recent review on the biology of hypoxia,[39] indicates that quantification of tumor hypoxia can be performed directly or indirectly, and with exogenous or endogenous markers. Tumor cells can launch various intracellular signaling pathways to survive hypoxia, such as HIF-1–mediated gene expression, the unfolded protein response, and AKT-mammalian target of rapamycin signaling. These pathways prompt aggressive, metastatic, and treatment-insensitive tumors and are considered potential targets for therapy. Hypoxia leads to important, but unfortunately not well-understood changes in microRNA expression, epigenetics (study of variations that are caused by external factors that switch genes on and off and affect how genes being read by cells), and metabolism.

Near-infrared fluorescence imaging has emerged as a sensitive tool for non-invasive cancer imaging,[20-28] and the use of nitroimidazoles as exogenous markers has received great attention because of their unique behavior in hypoxic environments owing to their high electron affinity. This is a well-studied class of molecular probes that target tumor hypoxia by nucleophilic covalent binding to proteins in environments of low pO2 (<1.5% O2).[29-33] A 2-nitroimidazole-indocyanine green (ICG) conjugate was recently reported to persist in the tumors for a significantly longer period than ICG as shown by NIR-fluorescence tomography,[29, 31, 32, 34-37] suggesting a possible application of the hypoxia selectivity of 2-nitroimidazole family for *in vivo* fluorescence imaging.

3-1.1 Nitroimidazole-piperazine-ICG

In an earlier study, the biodistribution of a new generation of hypoxia probe, 2-nitroimidazole ICG conjugate, with two carbon atoms less in the polyene linker was studied in

murine tumor model *in vivo*. The results were compared with an earlier version of the hypoxia probe that was synthesized with an ethanolamine linker. The *in vivo* experiments were conducted with balb/c mice and the new 2-nitroimidazole ICG conjugate showed more than twice the average *in vivo* fluorescence intensity in the tumor beyond two hours post injection as compared with the older version of the piperzine-2-nitroimidazole-ICG. These initial results suggested that the modified 2-nitroimidazole ICG may significantly improve *in vivo* tumor hypoxia targeting. [43] However, synthesizing 2-nitroimidazole ICG is a very complicated, time-consuming process and expensive. In order to overcome these obstacles, 4-nitroimidazole-ICG using piperazine linker to conjugate the 4-nitroimidazole and bis-carboxylic acid ICG (4-nitroimidazole-piperazine-ICG) moieties was synthesized for tumor hypoxia targeting using fluorescence imaging. The 4-nitro hypoxia conjugate is easier and considerably cheaper to make compared to the 2-nitro probe. The hypoxia targeting performance of the 4-nitroimidazole-piperazine-ICG hypoxia probe was compared with the previously tested 2-nitroimidazole-piperazine-ICG and imidazole-ICG in tumor bearing mouse model *in vivo* and data acquired validated the performance *in vitro* in tumor cells. Results with 4-nitroimidazole-piperazine-ICG had shown great potential and were had similar results compared to 2-nitroimidazole ICG.

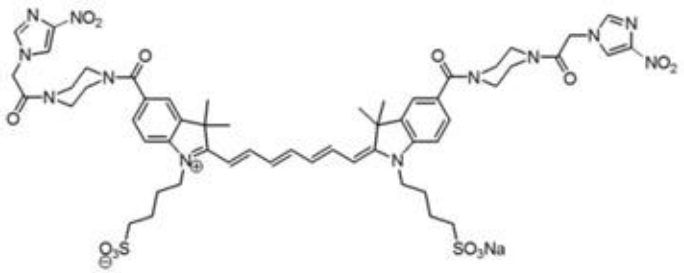

4-nitroimidazole piperazine-ICG

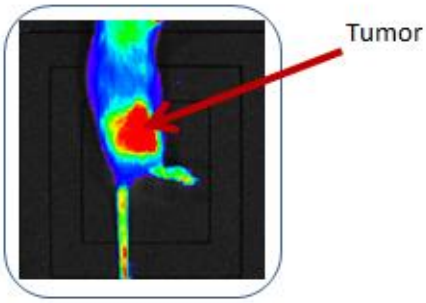

3-2 Synthesis of 4-nitroimidazole-ICG Dye Conjugates

In collaboration with the group of Prof. Michael Smith in the Department of Chemistry at the University of Connecticut, 4-nitroimidazole-ICG conjugate has been synthesized using piperazine linker to conjugate the 4-nitroimidazole and bis-carboxylic acid ICG (4-nitroimidazole-piperazine-ICG) moieties. Briefly, the 4-Nitroimidazole (1 g, 8.85 mmol) was added to a mixture of methyl bromoacetate (0.84 mL, 8.85 mmol), potassium carbonate (1.8 g, 13.27 mmol), and TBAI (0.070 g, 0.185 mmol) in 10 ml of acetonitrile. The mixture was heated to 80°C, and stirred vigorously at this temperature for 40 min. After cooling the ambient temperature, the inorganic salts were removed by vacuum filtration and washed with acetonitrile. The filtrate and washings were combined and the solvents evaporated in vacuo to give a residue that was recrystallized from ethyl acetate. (1.46 g, 7.87 mmol, 89%).Mp, 129-130°C. ^{1}H NMR (DMSO): δ 8.37 (s, ^{1}H), 7.82 (s, ^{1}H), 5.10 (s, ^{1}H); ^{13}C NMR (DMSO): δ 168.5, 147.3, 138.8, 123.0, 53.0, 48.7. [34]

UV-Vis absorption and fluorescence spectra for 4-nitroimidazole-ICG in **Figure 3-1** show a maximum absorption peak of 755 nm. The fluorescence spectra were detected with an excitation wavelength of 710 nm and had a maximum emission peak at 790 nm. The spectra shown were recorded using Varian Cary 50 UV-Vis spectrophotometer. The extinction coefficient for the 4-nitroimidazole-ICG conjugate is 207,519 $M^{-1}cm^{-1}$ and the calculated quantum yield is 0.07 as per the procedure discussed in section 1-1.3.

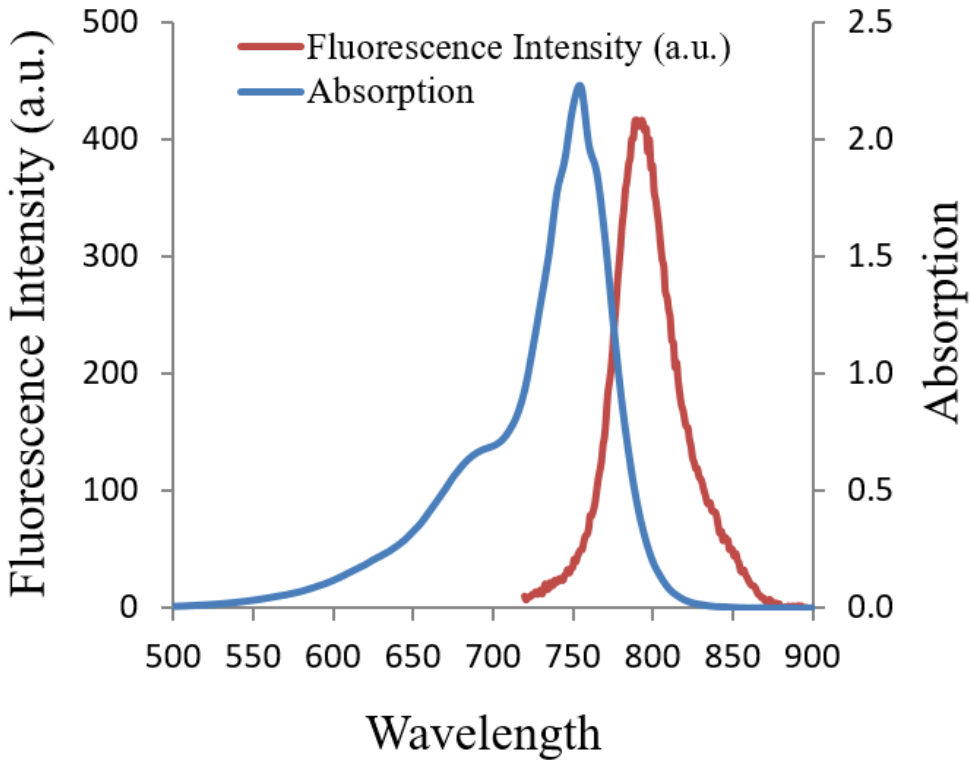

Figure 3-1 UV-Vis NIR absorption and fluorescence spectra for 4-nitroimidazole-ICG.

3-3 Methods and Procedures

3-3.1 *In vitro* Experiments

Hypoxia-dependent targeting of the dye was assessed *in vitro* using 4T1 breast cancer cells. Twelve dishes (T7425-2 60 mm x 15 mm surface-modified polystyrene tissue culture dishes (BD Falcon, Franklin Lakes, NJ, USA)), each having approximately 1 million tumor cells were evaluated. One group of six dishes was exposed to hypoxic conditions (5% CO_2, 1% O_2, 94% N_2, 37°C) by passing the gas mixture into a hypoxic chamber (Billups-Rothenberg, Inc., Del Mar, CA, USA) (**Figure 3-2**) for 10 min, the gas pressure was maintained at 5 psi throughout the 10

min passage and the chamber was then sealed and incubated for 15 h. The gas mixture was provided by Airgas East (Cheshire, Connecticut).

Figure 3-2 Hypoxic chamber

The second group of six dishes was incubated under normoxic conditions (5% CO_2, 95% O_2, 37°C) for the same period. Two dishes from each group were treated with 3 ml of 15 μM 4-nitroimidazole-ICG, two other dishes from each group were treated with 3 ml of 15 μM 2-nitroimidazole-ICG, and two other dishes from each group were treated with 3 ml of 15 μM imidazole-ICG. After the injection, the hypoxic group was put back into the hypoxic chamber under the same conditions mentioned previously and re-incubated both groups for 9 h. The medium was then removed and cells were rinsed with PBS to wash out free compounds and immediately both groups were taken for imaging using the Lumina II Imaging System. Cells

were then trypsinized to suspend the cells, and 2.5 ml of medium was added to each dish and then transferred to a spectroscopic grade cuvette. The fluorescence emission spectra was measured for each group using Varian Cary 50 UV-Vis spectrophotometer.

3-3.2 Tumor and Mice Imaging

In vivo tumor imaging experiments were performed using 4T1 Luc mammary carcinoma cells grown in 6-8 week old BALB/c female mice. The animal protocol was approved by the Institutional Animal Care and Use Committee of the University of Connecticut. 4T1 cells were cultured in 89% DMEM (Dulbecco's Modified Eagle Medium (1X)), 10% FBS (Fetal Bovine Serum, (Gibco, USA)) and 1% Pen/Strep (penicillin/streptomycin) and incubated at 37°C with 5% CO2. The 4T1 breast cancer cells were passed three times at 70% to 80% confluence in a T75 flask (BD Biosciences, Bedford, Massachusetts) prior to injection, and $1\times10\wedge5$ cells were administered by subcutaneous injection into the right flank of the mice. The experiments were performed when the tumor sizes reached approximately 7-8 mm in diameter.

Looking at the cultured dishes under the microscope confirms the status of the cultured cells visually. In **Figure 3-3** are three examples of cultured cells in three different stages, (a) Freshly passed cells (b) 70-80% confluence cultured cells and (c) Trypsinized cells (detached).

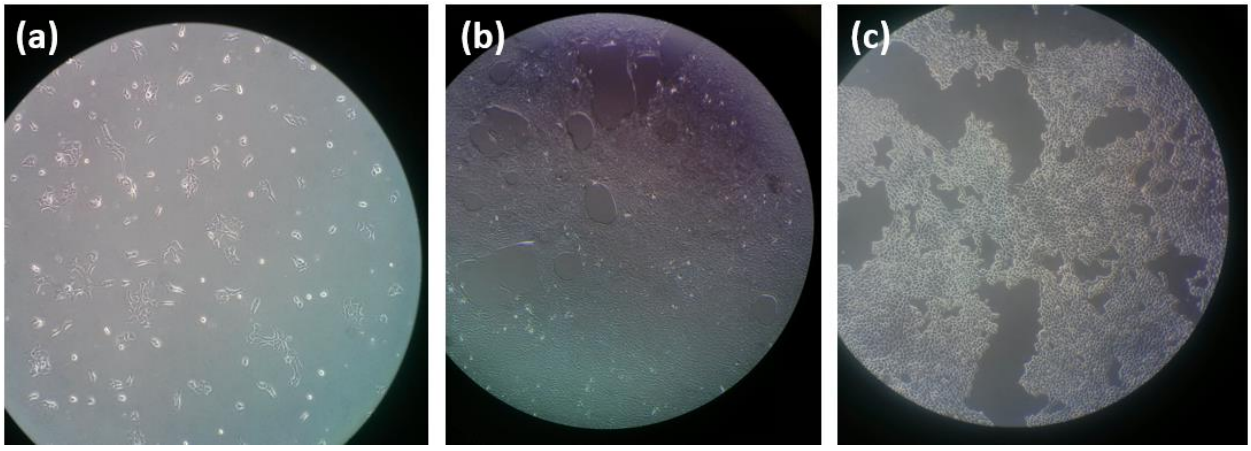

Figure 3-3 Cell culture examples

A group of five mice were injected intravenously through retro-orbital venous sinus with 100 µl of 4-nitroimidazole-ICG at 25 µM concentration. All injections and imaging experiments were done under anesthesia by inhalation of 1.5% isoflurane and 1 L/m O2. While lateral tail vein injection could be used for intravascular delivery of agents to mice, this procedure is technically challenging and often has a high rate of failure, hence, retro-orbital injection was chosen as an easier alternative reliable method for intravascular delivery of agents. Using IVIS Lumina II Imaging System (described later), the tumor of each mouse was imaged pre-injection, and then imaged for up to 60 min post-injection and then again at 2, 3, 4, 5, 6, 7, 8, 9, 10, 24 and 48 h. The mice were given a rest from anesthesia every hour. All animals recovered with no adversarial effects due to these injections. Fluorescence intensity was averaged and compared. After 48 h, mice were euthanized by cervical vertebra dislocation, and six organs including liver, spleen, kidneys, lungs, heart and the tumor tissue were excised from the mice. Organs were washed twice in PBS before acquiring florescence images for biodistribution analysis.

The tumors were imaged using an IVIS® Lumina II Imaging System (Caliper Life Sciences, Hopkinton, MA), which can provide visible light photographs and fluorescent images. The IVIS Lumina II is capable of imaging both fluorescent and bioluminescent reporters. The system is equipped with up to 21 filter sets that can be used to image reporters that emit from green to near-infrared. All imaging experiments were performed using a 745 nm excitation filter. The Living Image software yields high-quality, reproducible, quantitative results incorporating instrument calibration, background subtraction and image region of interest analysis algorithms (such as averaging, maximum and minimum, and brightness/contrast adjustment). The unit is equipped with gas anesthesia ports and 5 position manifold within imaging chamber allow anesthesia to be maintained during imaging sessions.

3-3.3 Immunohistochemistry (IHC)

Immunohistochemical staining was performed using the HypoxyprobePlus Kit (FITC-Mab) from HPI Inc, to visualize the hypoxia tumor areas using an IHC technique. As recommended by the protocol provided by HPI, 45 min before the animal was euthanized, 1.5 mg of HypoxyprobePlus Kit diluted in 100 µl of 0.9% saline solution was injected intravenously through retro-orbital venous sinus. Immediately after the animal was euthanized, the tumor specimens were collected and fast frozen directly in liquid nitrogen until cryosectioned into 10 µm sections. The prepared sections were stored in −80 °C before staining. After thawing, the sections were fixed in cold acetone for 10 min. Sections were incubated overnight at 4 °C with rabbit anti-pimonidazol anti sera PA2627 diluted 1:20 in PBS containing 0.1% bovine serum albumin and 0.1% Tween 20. The sections were then incubated for 60 min with FITC-conjugated goat anti-rabbit antibody. Between all steps of the staining procedure, the sections were rinsed

three times with PBS for 5 min each. Digital images of the stained sections were obtained using Zeiss Axio Imager M2 Microscope. The percentage of hypoxic areas was analyzed using the ImageJ program (National Institutes of Health, Bethesda, MD, http://rsb.info.nih.gov/ij/).

3-4 Results and Discussion

3-4.1 *In vitro* Hypoxia

The uptake of the dyes by both hypoxic and normoxic tumor cells was examined in culture dishes, and compared the results with the putative control imidazole ICG. All compounds were imaged using the Lumina II Imaging System described in the Experimental section. **Figure 3-4** shows one set of three dishes of the hypoxic group marked as (a) dish treated with 15 μM of imidazole ICG, (b) dish treated with 15 μM of 2-nitroimidazole-ICG and (c) dish treated with 15 μM of 4-nitroimidazole-ICG. The average radiant efficiency of the two separate sets was measured at 3.61 (±0.32)×107 and 3.27 (±0.30)×107 for 4-nitroimidazole-ICG and 2-nitroimidazole-ICG, respectively, compared to 1.79 (±0.4)×107 for the control dish of imidazole ICG. A graphical representation in **Figure 3-5** shows that dishes treated with 2-nitroimidazole-ICG and 4-nitroimidazole-ICG resulted in the detection of significantly higher levels of fluorescence in the cells cultured under hypoxia than those in cells cultured under normoxia conditions. The average radiant efficiency of 1.04 (±0.03) $\times 10^7$ and 1.22 (±0.11) $\times 10^7$ was measured for the 2-nitroimidazole-ICG and 4-nitroimidazole-ICG respectively. Images were retrieved using a 745 nm excitation filter. These results were encouraging to further study the efficacy of this probe attachment to hypoxic regions in vivo which will be discussed in the next chapter.

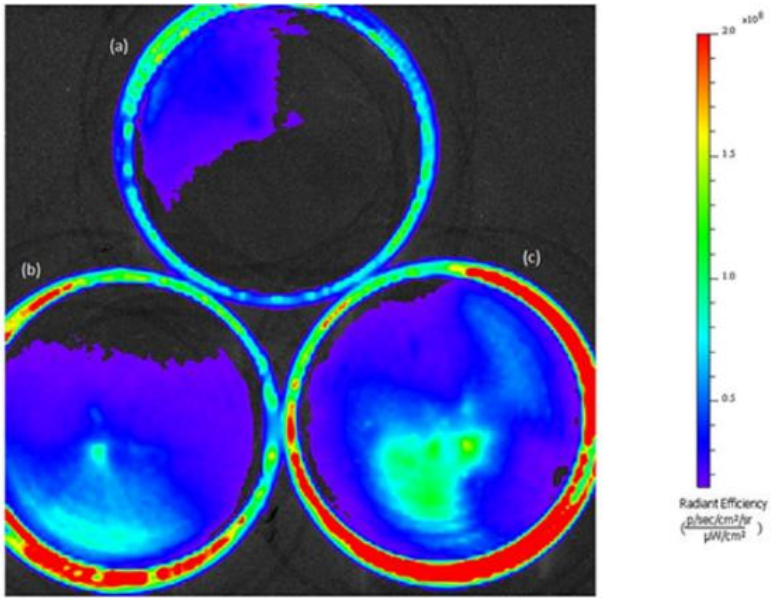

Figure 3-4 Fluorescence images of cultured 4T1 breast cancer cells under hypoxic conditions treated with (a) imidazole ICG, (b) 2-nitroimidazole-ICG, and (c) 4-nitroimidazole-ICG

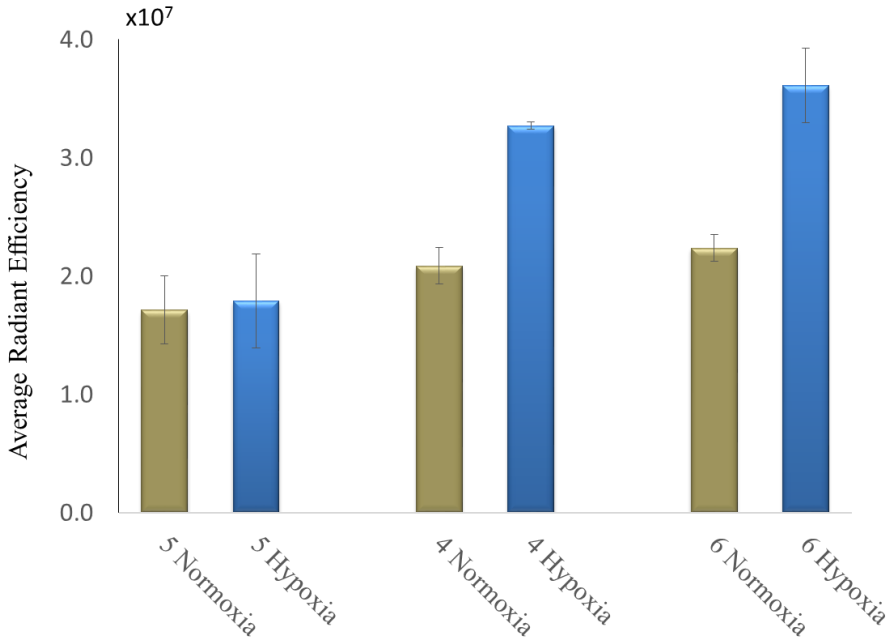

Figure 3-5 Graphical bars show average radiant efficiency of the hypoxic and normoxic dishes of the imidazole ICG (5), 2-nitroimidazole-ICG (4), and 4-nitroimidazole-ICG (6).

3-4.2 *In vivo* Imaging

Fluorescent images in **Figure 3-6** was taken using the IVIS® Lumina II Imaging System of the whole mouse body imaging over time (48 h) showing the accumulated uptake of the injected **(A)** 4-nitroimidazole-ICG, **(B)** 2-nitroimidazole-ICG and **(C)** Imidazole-ICG. The imaging system was set at a 745 nm excitation filter. Fluorescence radiation started to appear at one minute after injection and the radiant efficiency (Radiant efficiency, unit: p/sec/cm2/sr/(µW/cm2)) plateaued at 15 min post-injection. As **Figure 3-6 (A)** shows, injection with 4-nitroimidazole-ICG persisted for 48 hours and a residual trace was shown at 48 hours post injection which compared to 2-nitroimidazole-ICG injection on average performed even better as seen in **(B)**. While imidazole-ICG stayed in mice for about three hours and was washed away **(C).** The data was collected for the maximum radiation efficiency throughout the 48 h was quantitatively evaluated and expressed as the mean fluorescence signal (±sd), then compared to same concentration injection of 2-nitroimidazole-ICG and imidazole-ICG under the same conditions.

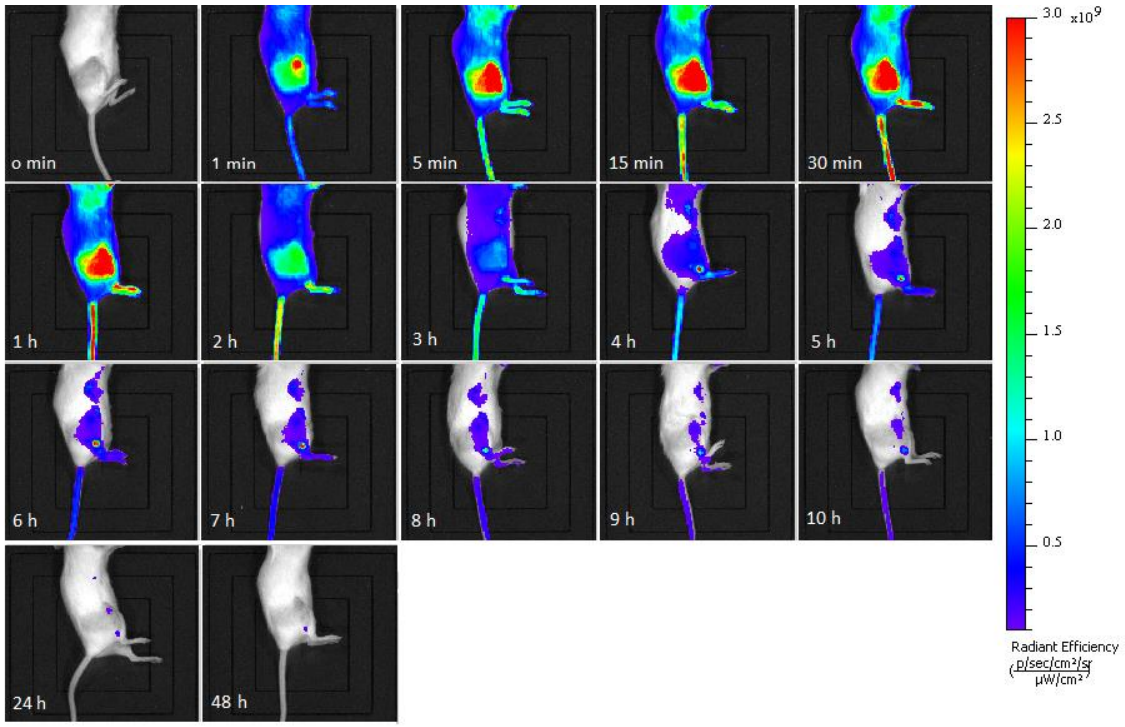
o min
1 min
5 min
15 min
30 min
1 h
2 h
3 h
4 h
5 h
6 h
7 h
8 h
9 h
10 h
24 h
48 h
3.0 x10^9
2.5
2.0
1.5
1.0
0.5
Radiant Efficiency
(p/sec/cm²/sr
µW/cm²)

(A)

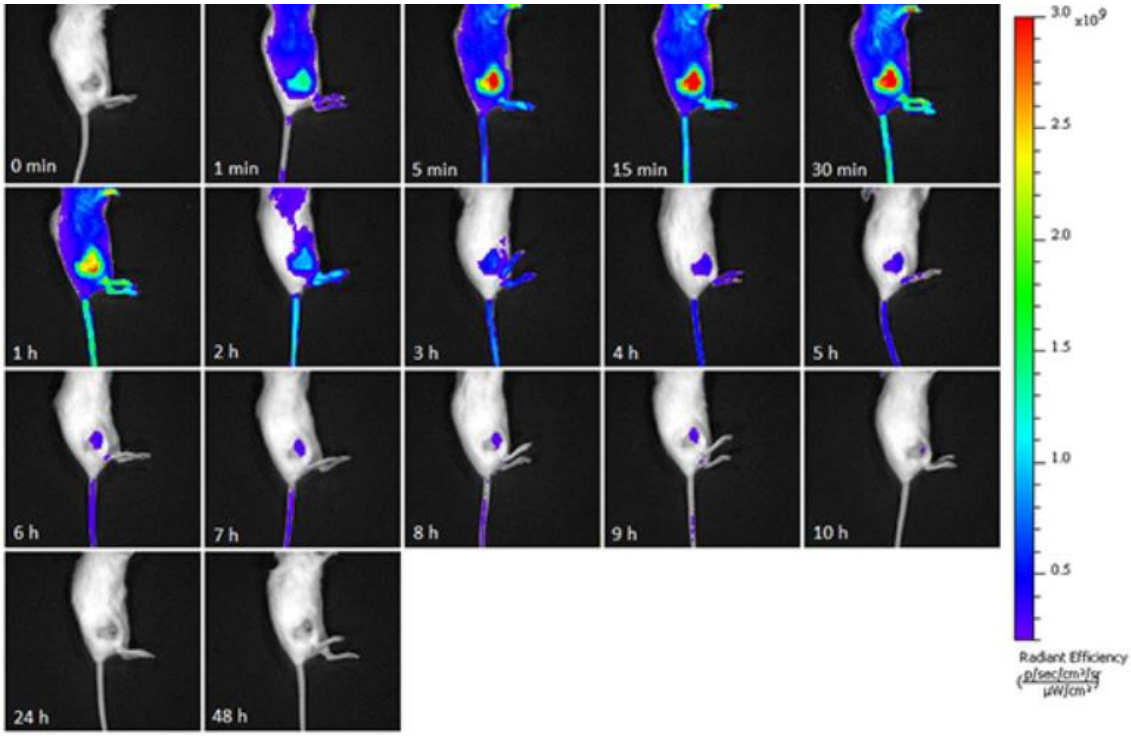
0 min
1 min
5 min
15 min
30 min
1 h
2 h
3 h
4 h
5 h
6 h
7 h
8 h
9 h
10 h
24 h
48 h
3.0 x10^9
2.5
2.0
1.5
1.0
0.5
Radiant Efficiency
(p/sec/cm²/sr
µW/cm²)

(B)

(C)

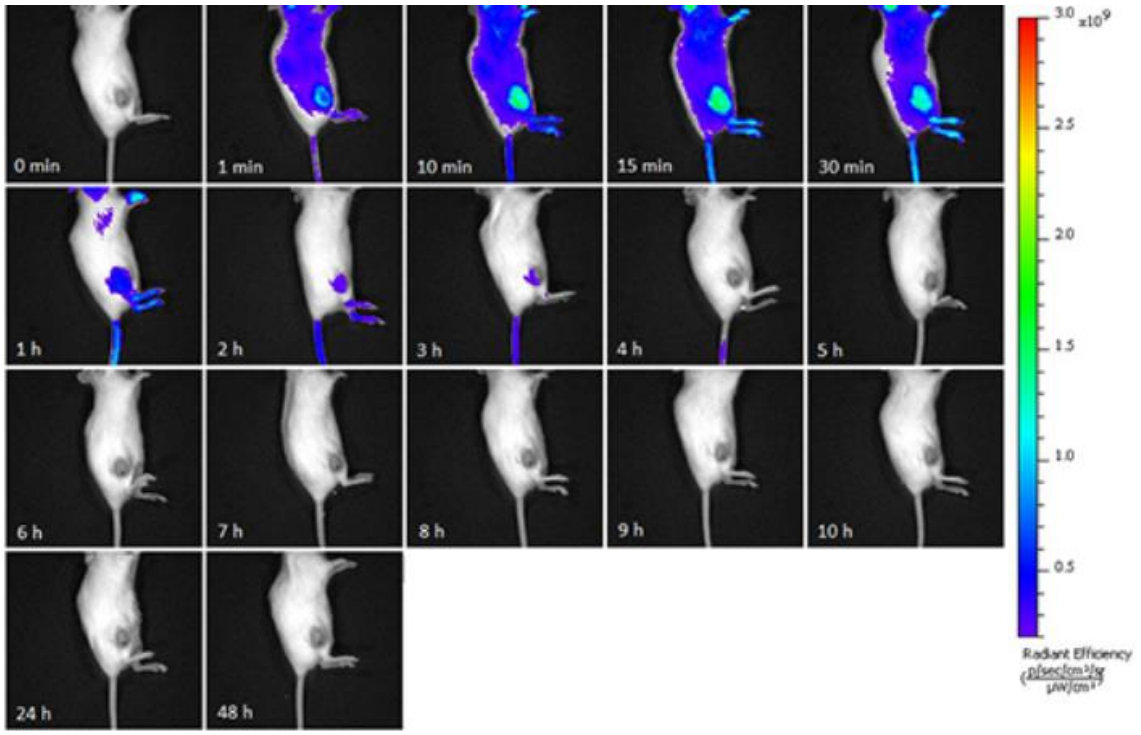

Figure 3-6 *In vivo* fluorescence distribution of a mouse injected with 100 µl at 25 µM concentration of (A) 4-nitroimidazole-ICG (B) 2-nitroimidazole-ICG and (C) Imidazole-ICG. (Image on top left is pre-injection and at 1, 5, 15, 30 min, 1 through 10 h, 24 and 48 h post-injection).

Table 3-1 and the graphical representation in **Figure 3-7** show the dye washout as a function of time comparing the three groups of nitroimidazole conjugates; the 4-nitroimidazole-ICG shows a higher fluorescent intensity with an uptake at about 1.5-fold over 2-nitroimidazole-ICG and about 2.5-fold over the imidazole-ICG at the 15 min peak post-injection. Maximum radiant efficiency for 4-nitroimidazole-ICG, 2-nitroimidazole-ICG and imidazole-ICG was measured at 5.05 (±0.57) $\times 10^9$, 3.39 (±0.33) $\times 10^9$ and 2.00 (±0.20) $\times 10^9$ respectively. Strong fluorescence intensity was still detected 3 hours post-injection at 91 and 69 times higher than the background for the 4-nitroimidazole-ICG and 2-nitroimidazole-ICG compared to 25 times for imidazole-ICG.

Based on these results, the efficacy of 4-nitroimidazole-ICG as a hypoxia targeting fluorescence probe has been proven to be effective and the dye was retained to a great extent in hypoxic tumors when compared with imidazole ICG derivative.

Comparisons between multiple groups were made with two-way ANOVA analyses. When comparing the radiation intensity between the three different conjugates using two-tail t-test, 4-nitrioimidazole-ICG was shown to have a slightly higher intensity than 2-nitrioimidazole-ICG. However, this increase was not statistically significant ($p > 0.05$). On the other hand, 4-nitroimidazole-ICG was shown to have a statistically significant increase in intensity when compared to imidazole-ICG, ($p < 0.05$).

Table 3-1 Radiant efficiency of the dye conjugates

Time	4 nitroimidazole-pip ($x10^9$)	2 nitroimidazole-pip ($x10^9$)	imidazole ICG ($x10^9$)
Background	0.009 (±0.001)	0.009 (±0.0004)	0.013 (±0.0014)
1 min	3.72 (±0.27)	1.57 (±0.18)	1.14 (±0.003)
15 min	5.05 (±0.57)	3.39 (±0.33)	2.00 (±0.20)
1 h	3.80 (±0.79)	2.95 (±0.46)	0.717 (±0.11)
3 h	0.84 (±0.28)	0.643 (±0.16)	0.347 (±0.21)
6 h	0.39 (±0.16)	0.295 (±0.06)	0.202 (±0.17)
9 h	0.29 (±0.09)	0.237 (±0.06)	0.0874 (±0.01)
24 h	0.17 (±0.08)	0.130 (±0.02)	0.0677 (±0.03)
48 h	0.1 (±0.05)	0.0971 (±0.02)	0.0486 (±0.02)

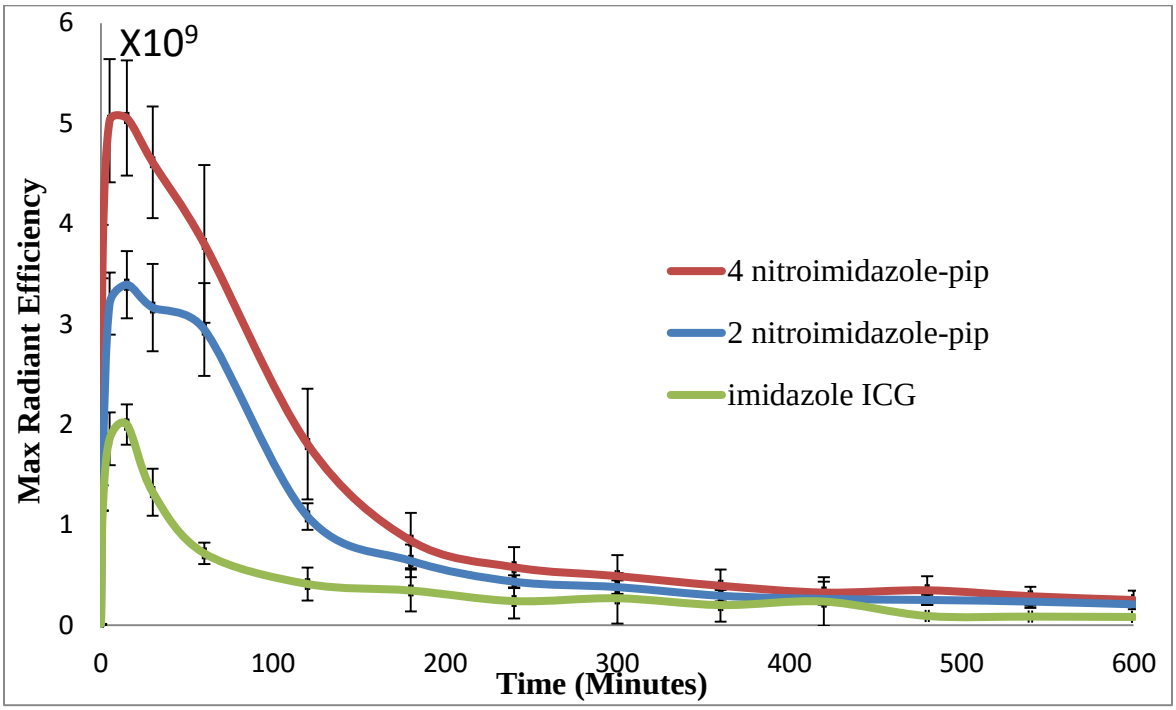

Figure 3-7 A graphical representation showing the washout as a function of time comparing the three groups of nitroimidazole conjugates, the 4-nitroimidazole-ICG shows a higher fluorescent intensity after 15 min post-injection.

3-4.3 Biodistribution Analysis

For dye accumulation and retention analysis in organs, mice were euthanized 48 h post-injection, and six organs were excised and imaged. Fluorescence intensity of tumor, heart, lungs, kidneys, spleen and liver were measured. **Figure 3-8** shows the average fluorescence intensity distribution in the organs calculated from all mice groups injected with 4-nitroimidazole-ICG, 2-nitroimidazole-ICG and imidazole-ICG, and results show a high retention in tumor and kidneys in both 4-nitroimidazole-ICG and 2-nitroimidazole-ICG due to slow loss of the dye conjugates from the tumor as a function of time with excretion via the kidney and liver. The mean value measured for maximum fluorescence intensity in tumor was 1.39 (±0.44) $\times 10^8$ for the group injected with 4-nitroimidazole-ICG and 1.8 (±0.77) $\times 10^8$ for the group injected with 2-nitroimidazole-ICG, these results are still two times higher than the imidazole-ICG which is in agreement with the *in vivo* measurements. **Figure 3-9** shows the fluorescence images of the major organs and tumor for the mice group injected with 4-nitroimidazole-ICG at 48 h (2-nitrioimidazole-ICG and imidazole-ICG images not shown). Using a two-tail t-test was performed between 4-nitrioimidazole-ICG and 2-nitrioimidazole-ICG *ex vivo* data groups and in agreement with our in-vivo data, there was no significant difference statistically ($p > 0.05$).

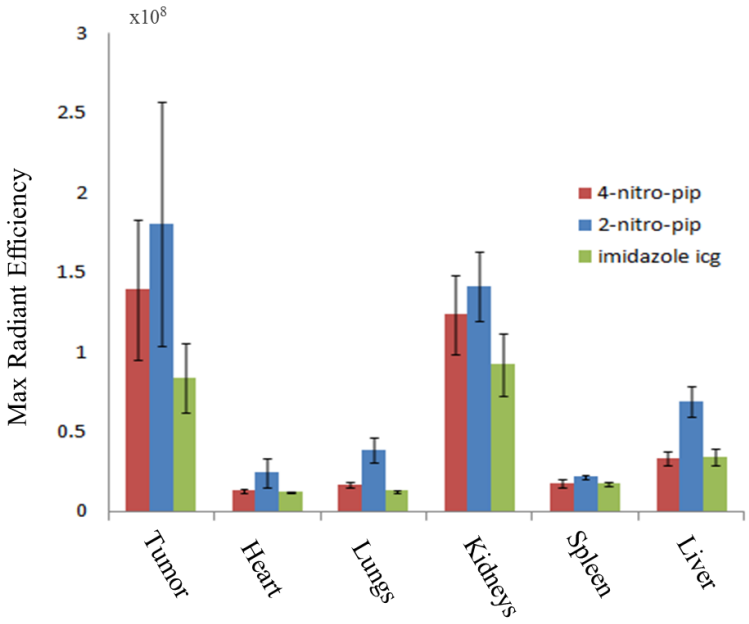

Figure 3-8 Biodistribution analysis of all mice groups bearing 4T1 tumors after retro-orbital venous sinus with 100 µl of 4-nitroimidazole-ICG, 2-nitroimidazole-ICG and imidazole-ICG. Bars represent the retention of the dye 48 h post-injection.

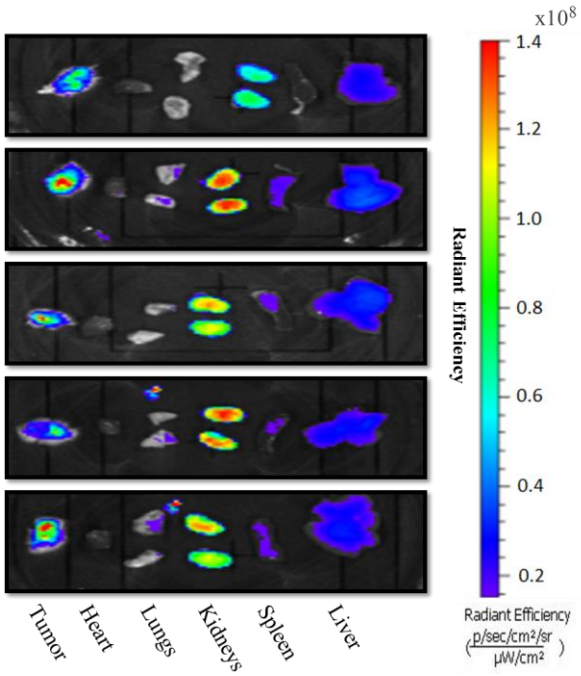

Figure 3-9 Fluorescence images show major organs and tumor for the mice group injected with 4-nitroimidazole-ICG at 48 h.

3-4.4 Immunohistochemistry

To determine the hypoxic status in various tumor groups, we obtained histology images of stained sections using Zeiss Axio Imager M2 microscope; images were analyzed using ImageJ to calculate the percentage of the hypoxic area. The percentage of the hypoxic area is defined as the number of pixels above the threshold in hypoxic areas, over the total number of pixels of the total area analyzed. We prepared four stained sections of each tumor. The average hypoxic area percentage from mice treated with 2-nitroimidazole-ICG, 4-nitroimidazole-ICG, and imidazole ICG was calculated at 1.6% (±0.011), 2.7% (±0.019) and 3% (±0.022) respectively. A representation of the data analysis is shown in **Figure 3-10**. These results show no statistical significant difference of hypoxic area percentage between the 4-nitroimidazole-ICG and 2-nitroimidazole-ICG ($p > 0.05$) and similarly 4-nitroimidazole-ICG and imidazole ICG hypoxic area percentage also showed no statistical significant difference ($p > 0.05$).

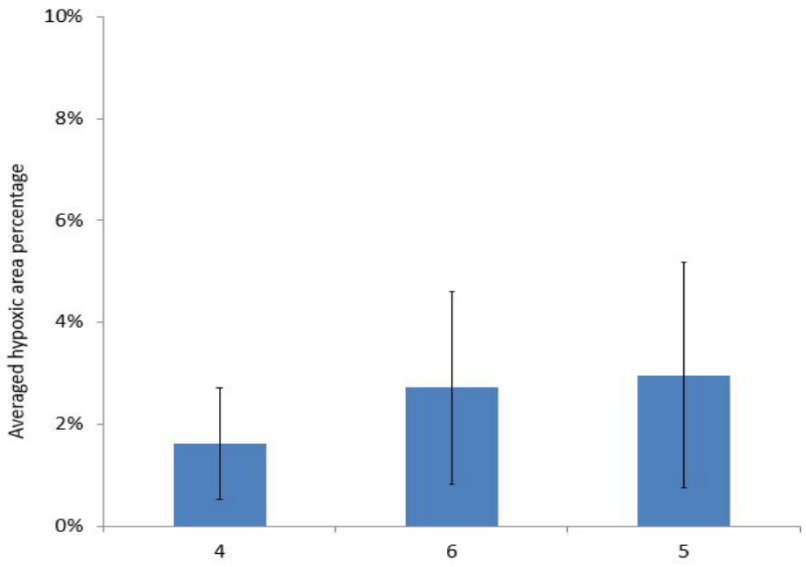

Figure 3-10 Averaged hypoxic area percentage calculated on all stained tumor slices (sectioned at 10μm) referenced as 2-nitroimidazole-ICG (4), 4-nitroimidazole-ICG (6), and imidazole ICG (5)

To validate differences in dye residual accumulation in each tumor, fluorescence images were obtained from commercial Li-COR imaging system and they are shown in **Figure 3-11**, with mice injected with (a) 2-nitroimidazole-ICG, (b) 4-nitroimidazole-ICG, and (c) imidazole ICG. Using ImageJ software, the average integrated fluorescence density over the tumor sample area was calculated and mean value of the four different slices in each group was measured at 54.3 (±10.1) and 50.6 (±9.8) for 2-nitroimidazole-ICG and 4-nitroimidazole-ICG, respectively, compared to 8.5 (±3.1) for imidazole ICG as shown in **Figure 3-12**. These results indicate similar fluorescence properties for both 4-nitroimidazole-ICG and 2-nitroimidazole-ICG. The difference of tumor-integrated density between 4-nitroimidazole-ICG and 2-nitroimidazole-ICG was not statistically significant ($p > 0.05$). However, significant difference was observed between 4-nitroimidazole-ICG and imidazole ICG ($p < 0.05$). This data confirms our *ex vivo* study and confirm dye residual in the tumor area.

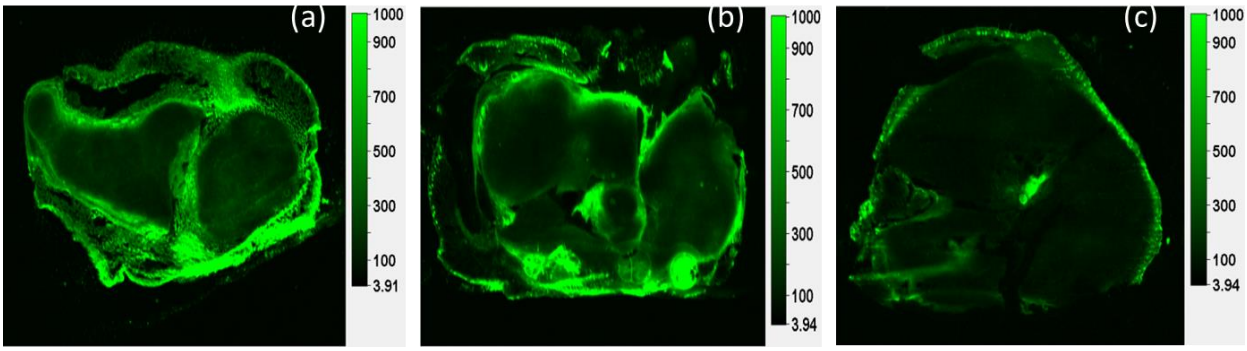

Figure 3-11 Li-COR images of 10 μm slices of mice tumors injected with (a) 2-nitroimidazole-ICG (4) (b) 4-nitroimidazole-ICG (6), and (c) imidazole ICG (5)

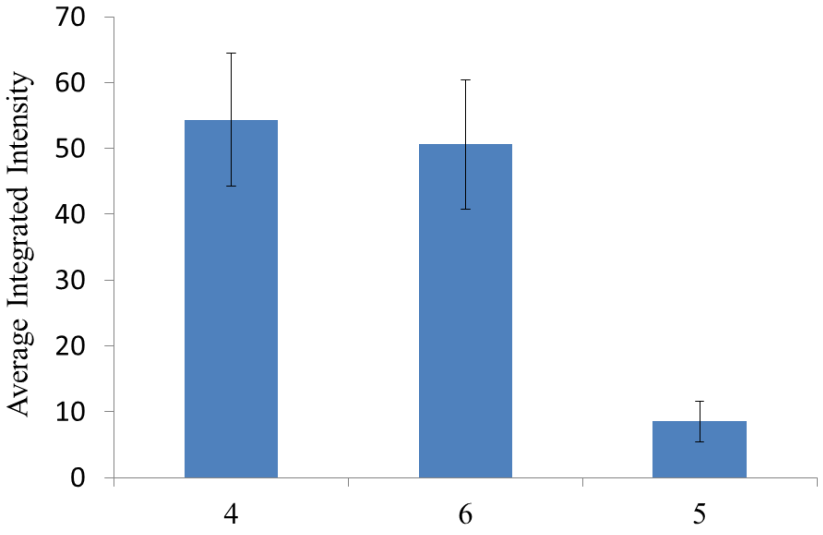

Figure 3-12 A graphical representation showing the average integrated density calculated for all stained slices imaged with Li-COR imager.

3-5 Summary

The results presented here demonstrate the feasibility of using the 4-nitroimidazole-ICG as a hypoxia targeting fluorescence probe. Despite the fact that 2-nitro derivatives have been shown to be the more useful derivatives for NIR fluorescence imaging of hypoxic tumors, the efficacy of 4-nitroimidazole-ICG as a hypoxia targeting fluorescence probe has been demonstrated. Li-COR imaging data analysis confirmed very similar fluorescence properties 4-nitroimidazole-ICG and 2-nitroimidazole-ICG. Analysis of data collected from tumor cells as well as that from the moue studies showed that both dye-conjugates were retained to a great extent in hypoxic tumors when compared with imidazole derivative, which is taken to be a realistic standard to probe the efficacy of each dye. However, the retention of the imidazole derivative in the tumors suggests that other factors are at work for uptake of the dye conjugates by the tumor. Further studies are required to illuminate this issue. The histology images of tumor stained sections confirm similar hypoxic condition of three mice groups.

Currently, 2-nitroimidizole sells for about $343.50/g whereas 4-nitroimidazole for $1.81/g, so the 2-nitroimdiazole is nearly 190 times as expensive on a per-gram basis [44]. The cost of 2-nitroimidazole is, therefore, nearly prohibitive for scale-up of the multi-step synthesis of our dye-conjugates. Based on price considerations alone, the preparation of a 4-nitroimidazole dye-conjugate was a worthy goal. However, there are concerns about the toxicity of 4-nitroimidazole derivatives as reported in earlier work. [45-46] Despite these reports, work by Wang and coworkers [47] as well as Zhang, Jin, and coworkers [48] showed that the preparation of 99mTc-labeled 4-nitroimidazole complexes for imaging tumor hypoxia was feasible, and they reported positive results.

A cytotoxicity was not performed at this current work, but it is would be required if 4-nitroimidazole-piperazine-ICG is to be pursed as a useful imaging agent. However, no observable difference for the mice injected with either of the three dyes based on post-injection activity or weight loss, suggesting that there is no significant short-term toxicity was noticed.

3-6 References

1. Hanahan, D. and R.A. Weinberg, *The hallmarks of cancer.* Cell, 2000. 100(1): p. 57-70.

2. Vaupel, P., F. Kallinowski, and P. Okunieff, *Blood flow, oxygen and nutrient supply, and metabolic microenvironment of human tumors: a review.* Cancer Res, 1989. 49(23): p. 6449-65.

3. Brown, J.M. and A.J. Giaccia, *The unique physiology of solid tumors: opportunities (and problems) for cancer therapy.* Cancer Res, 1998. 58(7): p. 1408-16.

4. Thomlinson, R. and L. Gray, *The Histological Structure of Some Human Lung Cancers and the Possible Implications for Radiotherapy.* Br J Cancer, 1955. 9(4): p. 539–549.

5. Nunn, A., K. Linder, and H.W. Strauss, *Nitroimidazoles and imaging hypoxia.* Eur J Nucl Med, 1995. 22(3): p. 265-80.

6. Fernandez, S., et al., *Synthesis, in vitro and in vivo characterization of two novel 68Ga-labelled 5-nitroimidazole derivatives as potential agents for imaging hypoxia.* Nucl Med Biol, 2013. 40(2): p. 273-9.

7. Zheng, X., et al., *Hypoxia-specific ultrasensitive detection of tumours and cancer cells in vivo.* Nat Commun, 2015. 6: p. 5834.

8. Chitneni, S.K., et al., *Molecular imaging of hypoxia.* J Nucl Med, 2011. 52(2): p. 165-8.

9. Ogawa, M., et al., *In vivo molecular imaging of cancer with a quenching near-infrared fluorescent probe using conjugates of monoclonal antibodies and indocyanine green.* Cancer Res, 2009. 69(4): p. 1268-72.

10. McCann, T.E., et al., *The use of fluorescent proteins for developing cancer-specific target imaging probes.* Methods Mol Biol, 2012. 872: p. 191-204.

11. Luo, S., et al., *A review of NIR dyes in cancer targeting and imaging.* Biomaterials, 2011. 32(29): p. 7127-38.

12. Alander, J.T., et al., *A review of indocyanine green fluorescent imaging in surgery.* Int J Biomed Imaging, 2012. 2012: p. 940585.

13. Harada, T., et al., *Activatable organic near-infrared fluorescent probes based on a bacteriochlorin platform: synthesis and multicolor in vivo imaging with a single excitation.* Bioconjug Chem, 2014. 25(2): p. 362-9.

14. Pauli, J., et al., *An in vitro characterization study of new near infrared dyes for molecular imaging.* Eur J Med Chem, 2009. 44(9): p. 3496-503.

15. Kai Licha, B.R., Vasilis Ntziachristos, Andreas Becker, Britton Chance and and W. Semmler, *Hydrophilic Cyanine Dyes as Contrast Agents for Near-infrared Tumor.* Photochemistry and Photobiology, 2000. 72(3): 392–398.

16. Pauli, J., et al., *Novel fluorophores as building blocks for optical probes for in vivo near infrared fluorescence (NIRF) imaging.* J Fluoresc, 2010. 20(3): p. 681-93.

17. Weissleder, R., *Molecular imaging in cancer.* Science, 2006. 312(5777): p. 1168-71.

18. Contag, C.H., *In vivo pathology: seeing with molecular specificity and cellular resolution in the living body.* Annu Rev Pathol, 2007. 2: p. 277-305.

19. Green, A.H., et al., *In vitro testing of a protease-sensitive contrast agent for optoacoustic imaging.* J Biomed Opt, 2010. 15(2): p. 021315.

20. Wu, J.B., et al., *Near-infrared fluorescence imaging of cancer mediated by tumor hypoxia and HIF1alpha/OATPs signaling axis.* Biomaterials, 2014. 35(28): p. 8175-85.

21. James, N.S., et al., *Evaluation of polymethine dyes as potential probes for near infrared fluorescence imaging of tumors: part - 1.* Theranostics, 2013. 3(9): p. 692-702.

22. Srivatsan, A., et al., *Gold nanocage-photosensitizer conjugates for dual-modal image-guided enhanced photodynamic therapy.* Theranostics, 2014. 4(2): p. 163-74.

23. Frangioni, J.V., *In vivo near-infrared fluorescence imaging.* Curr Opin Chem Biol, 2003. 7(5): p. 626-34.

24. E. M. Sevick-Muraca*, G.L., J. S. Reynolds, T. L. Troy and C. L. Hutchinson, *Fluorescence and Absorption Contrast Mechanisms for Biomedical Optical Imaging Using Frequency-Domain Techniques.* Photochemistry and Photobiology, 1997. 66(1): 55-64.

25. Biswal, N.C., et al., *Fluorescence imaging of vascular endothelial growth factor in tumors for mice embedded in a turbid medium.* J Biomed Opt, 2010. 15(1): p. 016012.

26. Weissleder, R., et al., *In vivo imaging of tumors with protease-activated near-infrared fluorescent probes.* Nat Biotechnol, 1999. 17(4): p. 375-8.

27. Wu, J., D. Pan, and L.W. Chung, *Near-infrared fluorescence and nuclear imaging and targeting of prostate cancer.* Transl Androl Urol, 2013. 2(3): p. 254-264.

28. Dobosz, M., et al., *Noninvasive measurement of pharmacokinetics by near-infrared fluorescence imaging in the eye of mice.* J Biomed Opt, 2014. 19(1): p. 16022.

29. Xu, Y., et al., *Targeting tumor hypoxia with 2-nitroimidazole-indocyanine green dye conjugates.* J Biomed Opt, 2013. 18(6): p. 66009.

30. Okuda, K., et al., *2-Nitroimidazole-tricarbocyanine conjugate as a near-infrared fluorescent probe for in vivo imaging of tumor hypoxia.* Bioconjug Chem, 2012. 23(3): p. 324-9.

31. Biswal, N.C., et al., *Imaging tumor hypoxia by near-infrared fluorescence tomography.* J Biomed Opt, 2011. 16(6): p. 066009.

32. Kizaka-Kondoh, S. and H. Konse-Nagasawa, *Significance of nitroimidazole compounds and hypoxia-inducible factor-1 for imaging tumor hypoxia.* Cancer Sci, 2009. 100(8): p. 1366-73.

33. Hodgkiss, R.J., *Use of 2-nitroimidazoles as bioreductive markers for tumour hypoxia.* Anticancer Drug Des, 1998. 13(6): p. 687-702.

34. Pavlik, C., et al., *Synthesis and fluorescent characteristics of imidazole–indocyanine green conjugates.* Dyes and Pigments, 2011. 89(1): p. 9-15.

35. Youssif, B.G., et al., *Development of a hypoxia-selective near-infrared fluorescent probe for non-invasive tumor imaging.* Chem Pharm Bull (Tokyo), 2012. 60(3): p. 402-7.

36. Li, Z. and T. Chu, *Recent advances on radionuclide labeled hypoxia-imaging agents.* Curr Pharm Des, 2012. 18(8): p. 1084-97.

37. Tricia Melo, J.D., James R. Ballinger, A. Michael Rauth, *<BRU5 9-2 1 a Second-Generation 99mTc@Labe1ed 2-Nitroimidazole for Imaging Hypoxia in Tumors.pdf>*. J NucI Med, 2000; (41): p. 169-176.

38. Li, X., et al., *Effect of hypoxia/reoxygenation on CD73 (ecto-5'-nucleotidase) in mouse microvessel endothelial cell lines.* Microvasc Res, 2006. 72(1-2): p. 48-53.

39. Span, P. N. and J. Bussink (2015). "*Biology of hypoxia*." Semin Nucl Med 45(2): 101-109.

40. Cai, Q., T. Yu, et al. (2015). "*A turn-on fluorescent probe for tumor hypoxia imaging in living cells*." Chem Commun (Camb) 51(79): 14739-14741.

41. Brown, J. M. and W. R. Wilson (2004). "*Exploiting tumour hypoxia in cancer treatment*." Nat Rev Cancer 4(6): 437-447.

42. Vaupel, P. and A. Mayer (2007). "Hypoxia in cancer: significance and impact on clinical outcome." Cancer Metastasis Rev 26(2): 225-239.

43. Zhou, F., S. Zanganeh, et al. (2015). "Targeting tumor hypoxia: a third generation 2-nitroimidazole-indocyanine dye-conjugate with improved fluorescent yield." Org Biomol Chem 13(46): 11220-11227.

44. Sigma-Aldrich Chemical Co. data. See http://www.sigmaaldrich.com/catalog/product/aldrich/195650?lang=en&region=US

45. Stratford IJ, Williamson C, Hardy C. Cytotoxic properties of a 4-nitroimidazole (NSC 38087), a radiosensitizer of hypoxic cells in vitro. Br J Cancer 1981; 44: 109-116;

46. Chan PKL, Skov KA, James BR. Further studies on toxic and radiosensitizing properties of ruthenium complexes of 4-nitroimidazoles. Int J Radiat Biol 1987; 52: 49-55.

47. Chu T, Hu S, Wei, B, Yang Y, Liu X, Wang X. Synthesis and biological results of the 99mTc - labeled 4-nitroimidazole for imaging tumor hypoxia. Bioorg Med Chem Lett 2004; 14: 747-749.

48. Li Z, Zhang J, Jin Z, Zhang W, Zhang Y. Synthesis and biodistribution of novel 99mTc labeled 4-nitroimidazole dithiocarbamate complexes as potential agents to target tumor hypoxia. Med Chem Commun 2015; 6: 1143-1148.